Decaying turbulence in a stratified fluid of high Prandtl number

Shinya Okino[1],[†] and Hideshi Hanazaki[1]

[1]Department of Mechanical Engineering and Science, Kyoto University, Kyoto 615-8540, Japan

Decaying turbulence in a density-stratified fluid with a Prandtl number up to $Pr = 70$ is investigated by direct numerical simulation. In turbulent flow with a Prandtl number larger than unity, it is well known that the passive scalar fluctuations cascade to scales smaller than the Kolmogorov scale, and show the k^{-1} spectrum in the viscous–convective range, down to the Batchelor scale. In decaying stratified turbulence, the same phenomenon is initially observed for the buoyant scalar of high $Pr \ (= 70)$, until the Ozmidov scale becomes small and the buoyancy becomes effective even at the Kolmogorov scale. After that moment, however, the velocity components near the Kolmogorov scale begin to show strong anisotropy dominated by the vertically sheared horizontal flow, which reduces the vertical scale of density fluctuations. An analysis similar to that of Batchelor (*J. Fluid Mech.*, vol. 5, 1959, pp. 113–133) indeed shows that the vertically sheared horizontal flow reduces the vertical scale of density fluctuations, without changing the horizontal scale.

Key words: internal waves, stratified turbulence, turbulence simulation

1. Introduction

Transport of scalars, such as heat, salt and pollutants, by fluid flow is a universal phenomenon in nature, and is of importance in geophysics and engineering. The key parameter that characterises the diffusivity of those scalars is the Prandtl number $Pr = \nu^*/\kappa^*$, which is defined by the ratio of the kinematic viscosity ν^* of fluid to the diffusion coefficient κ^* of the scalar. (In this study, variables with or without an upper asterisk denote dimensional or non-dimensional quantities, respectively.) Since the diffusion coefficient of a substance in a liquid is generally much smaller than that of heat, the corresponding Prandtl number is much higher. For example, the value of Pr for salt in water is 700, and the passive scalars in water often have even higher Prandtl numbers of order 10^3, while the Prandtl number for thermal diffusion in water is only 7.

For turbulent stratified flows, the eddy viscosity and eddy diffusivity are often used instead of their molecular values to model the effects of turbulent mixing that occur at unresolved small scales. For example, ocean circulation models parametrise the small-scale diffusion, often using the same value of turbulent eddy diffusivity for

† Email address for correspondence: okino.shinya.8n@kyoto-u.ac.jp

heat and salt. With the intention to investigate the effects of 'differential diffusion' of scalars, Gargett, Merryfield & Holloway (2003) numerically simulated the turbulence in a fluid stratified by both heat and salt, using different molecular-diffusion coefficients ($Pr = 7$ and 70) for the two scalars. They showed that the turbulent diffusivity of the scalar of $Pr = 7$ exceeds that of $Pr = 70$ by 6 %–22 %, and argued that the difference of the turbulent diffusivity in seawater ($Pr = 7$ and 700) would be even larger. While there is an uncertainty in the relation between the molecular and turbulent diffusion, the thermohaline circulation predicted by the geophysical fluid dynamics laboratory (GFDL) ocean model is indeed very sensitive to the ratio of the turbulent eddy diffusivity between temperature and salinity (Gargett & Holloway 1992). Therefore, we need to know the effect of molecular diffusivity on the structure of stratified turbulence, especially at high Prandtl numbers.

The behaviour of small-scale fluctuations of a high-Prandtl-number scalar has been investigated theoretically by Batchelor (1959), assuming that the scalar is passive, i.e. the scalar does not contribute to the fluid density and the buoyancy force is absent. Batchelor showed that the scalar dissipates at the length scale of $L_B^* = Pr^{-1/2}L_K^*$, and the scalar variance spectrum is proportional to k^{*-1} in the viscous–convective subrange ($1/L_K^* < k^* < 1/L_B^*$). The scale $L_K^* = (\nu^{*3}/\epsilon_K^*)^{1/4}$ is the Kolmogorov scale (ϵ_K^* is the dissipation rate of kinetic energy) and L_B^* is now called the Batchelor scale. Batchelor's k^{-1} spectrum has actually been observed in a water channel experiment by Gibson & Schwarz (1963) and in oceanic measurements by Grant *et al.* (1968).

In a three-dimensional direct numerical simulation (DNS) of the forced isotropic turbulence, Bogucki, Domaradzki & Yeung (1997) found the k^{-1} power spectrum for passive scalars with a Prandtl number up to 7, showing the applicability of Batchelor's prediction even when the Reynolds number was not very high, i.e. when the microscale Reynolds number $Re_\lambda = u_{rms}^*\lambda^*/\nu^*$ is 77, where u_{rms}^* is the root-mean-square (r.m.s.) turbulent velocity and λ^* is the Taylor microscale. Batchelor (1959) indeed argues in his original paper that his scalar spectrum ($\propto k^{-1}$) below the Kolmogorov scale does not require a high Reynolds number, which would realise an inertial subrange in the kinetic-energy spectrum. Yeung, Xu & Sreenivasan (2002) subsequently performed a DNS of forced isotropic turbulence with a uniform mean scalar gradient, and found that the scalar shows the k^{-1} power spectrum at a higher Prandtl number ($Pr = 64$) but with a low Reynolds number ($Re_\lambda = 38$). Yeung *et al.* (2004) obtained the similar results with even higher Pr ($= 1024$) and lower Re_λ ($= 8$).

The above results are all for a passive scalar in isotropic turbulence. In stratified fluids, the distribution of the active scalars such as salt generates the buoyancy force, and the scalars behave differently from passive scalars. In the studies of decaying stratified turbulence, the suppression of vertical motion due to the exchange between the vertical kinetic energy and the potential energy has been observed in both experiments (e.g. Webster 1964; Lin & Pao 1979) and DNS (e.g. Riley, Metcalfe & Weissman 1981; Métais & Herring 1989). After the initial fluctuations have decayed, the buoyancy Reynolds number ($Re_b = \epsilon_K^*/(\nu^*N^{*2})$ with N^* being the Brunt–Väisälä frequency) becomes small, and the turbulence eventually takes a horizontally layered structure, which is often called a pancake vortex (e.g. Pao 1973; Métais & Herring 1989; Fincham, Maxworthy & Spedding 1996; Kimura & Herring 1996). Majda & Grote (1997) obtained a similar pancake structure as an exact solution of the linear advection–diffusion equations, in modelling the low-Froude-number limiting dynamics. The Froude number was a measure of the ratio between the Brunt–Väisälä period and the eddy turnover time, and was defined by $Fr = U^*/(N^*L^*)$, with U^* being the characteristic velocity and L^* the characteristic length.

In a salt-stratified water channel ($Pr = 700$), evolution of the grid-generated turbulence has been investigated at moderate mesh Froude numbers of order 10^1 (Stillinger, Helland & Van Atta 1983; Itsweire, Helland & Van Atta 1986). The transition from isotropic turbulence to flow with internal waves was observed when the Ozmidov scale $L_O^* = (\epsilon_K^*/N^{*3})^{1/2}$ decreased below the integral scale, where the Ozmidov scale is the scale above which the stratification effect is significant (Ozmidov 1965). In wind tunnel experiments for thermally stratified turbulence ($Pr \sim 0.7$), Lienhard & Van Atta (1990) have shown that the counter-gradient vertical density flux (i.e. conversion of potential energy into kinetic energy) is weaker for a lower Prandtl number. The difference between thermally stratified water ($Pr \sim 6$) and salt-stratified water ($Pr \sim 600$) was investigated by Komori & Nagata (1996). They realised the same initial disturbance using the same turbulence grid, but still found that a higher Prandtl number generates a stronger and smaller-scale counter-gradient flux. This Prandtl-number dependence could be explained also by linear processes (Hanazaki & Hunt 1996). The low-Froude-number turbulence was realised in the long-time development of the flow generated by a rake in a salt-stratified fluid (Fincham *et al.* 1996; Praud, Fincham & Sommeria 2005), and the vertical shearing of horizontal flow, which dominates the kinetic-energy dissipation, was found.

Recently, the decaying stratified turbulence at $Pr = 1$ with initially high Reynolds numbers has been simulated by Bartello & Tobias (2013) and Maffioli & Davidson (2016). In those papers, the theory of strongly stratified turbulence (Lindborg 2006) is examined, and the horizontal spectra of horizontal kinetic energy and potential energy in the inertial range are shown to follow the Kolmogorov and the Corrsin–Obukhov spectrum if the buoyancy Reynolds number is $O(10)$ or larger. Recent studies on forced stratified turbulence (e.g. de Bruyn Kops 2015; Maffioli, Brethouwer & Lindborg 2016; Maffioli 2017) also achieved a high Reynolds number ($Re_\lambda \gtrsim 400$), for which the $k^{-5/3}$ spectrum in kinetic energy was observed.

However, there have been only a few numerical studies intended for a Prandtl number larger than unity, due to the difficulty in resolving the very small Batchelor scales at high Prandtl numbers, while we know that the simulation at $Pr \sim 700$ is necessary for direct comparison with the salt-water experiments. The counter-gradient scalar flux, which is stronger for $Pr = 2$ than for $Pr = 1$, has been observed in DNS by Gerz & Yamazaki (1993). They argued that the potential energy of a high-Pr ($Pr > 1$) scalar would not be dissipated directly by its molecular diffusion, but would first be converted into kinetic energy and then dissipated by viscosity. The turbulence triggered by Kelvin–Helmholtz instability in an initially two-layer fluid was computed by Smyth (1999), and the dissipation-range scalar spectrum at Prandtl numbers as high as 7 was investigated. The results showed that the spectral form of the scalar dissipation agrees better with the spectrum proposed by Kraichnan (1968) than with that by Batchelor (1959), with similarity to the results for passive scalars (e.g. Bogucki *et al.* 1997). More recently, Salehipour, Peltier & Mashayek (2015) investigated the Prandtl-number dependence ($1 \leqslant Pr \leqslant 16$) of a turbulent mixing layer caused by the Kelvin–Helmholtz instability, and suggested the possibility of an 'ultraviolet catastrophe' in the limit of high Pr, where a very abrupt transition to turbulence occurs due to a direct and simultaneous injection of energy into all scales of motion. In their subsequent paper (Salehipour & Peltier 2015), they reformulated the diapycnal diffusivity, and showed that the corresponding turbulent Prandtl number decreases monotonically with the buoyancy Reynolds number Re_b.

In this paper we describe the results of a DNS of decaying stratified turbulence at Prandtl numbers up to 70, with a higher resolution (up to 2048^3 grid points) than
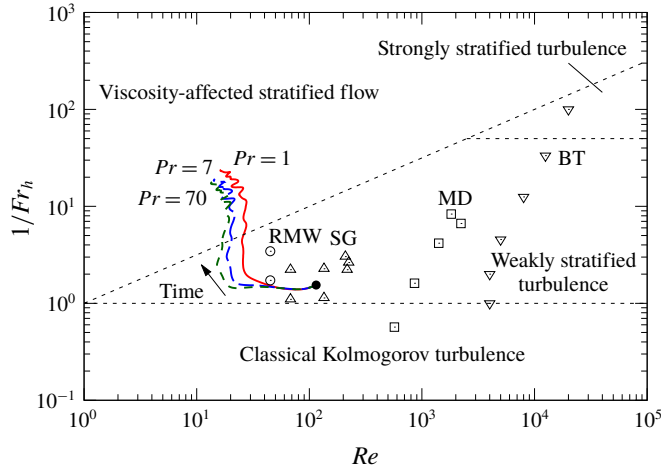
FIGURE 1. (Colour online) Reynolds number Re and inverse horizontal Froude number $1/Fr_h$ in decaying stratified turbulence analysed by DNS. Symbols show the initial values, i.e. the values when the kinetic-energy dissipation rate becomes maximum and small-scale velocity fluctuations have fully developed: ●, present study; ○, Riley *et al.* (1981) (RMW); △, Staquet & Godeferd (1998) (SG); ▽, Bartello & Tobias (2013) (BT); □, Maffioli & Davidson (2016) (MD). Temporal variations of parameters in the present study are shown by three curves ($Pr = 1$, 7 and 70, from right to left). The classification into four regimes is due to Brethouwer *et al.* (2007). The buoyancy Reynolds number becomes unity ($Re_b = Re\,Fr_h^2 = 1$) on the oblique dotted line.

the previous numerical simulations. This will realise conditions more similar to the salt-stratified experiments ($Pr \sim 700$) compared to the previous numerical studies, which were intended mostly for $Pr \leqslant 7$. The number of grid points necessary to resolve the smallest scale of a scalar fluctuation in turbulent flow is estimated by $(L^*/L_B^*)^3 = (L^*/L_K^*)^3(L_K^*/L_B^*)^3 \sim Re^{9/4}Pr^{3/2}$ (L^* being the integral scale), where the Reynolds number is defined by $Re = U^{*4}/(\nu^*\epsilon_K^*)$, with U^* being the mean horizontal velocity. Therefore, as long as the grid resolution L^*/L_B^* is the same, $Re\,Pr^{2/3}$ is constant, showing that the maximum attainable Reynolds number for a simulation with $Pr = 70$ becomes $70^{2/3}$ (~ 17) times smaller than that with $Pr = 1$. Then, our Reynolds number (figure 1) would become one order of magnitude smaller than that of Maffioli & Davidson (2016), who also used 2048 grid points in the horizontal direction. On the other hand, our Reynolds number is close to that of Staquet & Godeferd (1998), while the grid resolution is eight times higher than theirs (256^3 grid points). Then, the Prandtl number can be increased approximately up to 8^2 ($= 64$). Brethouwer *et al.* (2007) argued that the parameter map in figure 1 can be divided into four regimes, i.e. classical Kolmogorov turbulence ($Fr_h > 1$), weakly stratified turbulence ($Re_b = Re\,Fr_h^2 > 1$ and $0.02 < Fr_h < 1$), strongly stratified turbulence ($Re_b = Re\,Fr_h^2 > 1$ and $Fr_h < 0.02$), and viscosity-affected stratified flow ($Re_b = Re\,Fr_h^2 < 1$), where the horizontal Froude number is defined by $Fr_h = \epsilon_K^*/(N^*U^{*2})$. Our simulations start from the weakly stratified turbulence regime, and enter the viscosity-affected stratified flow regime. Therefore, after the turbulence has decayed, a clear dependence on the molecular effects of the Prandtl number would be observed.

We will show first the Prandtl-number dependence of the statistical quantities such as energies and vertical density flux (§ 3.1), then investigate the spatial distribution

of density fluctuations, which exhibits vertically small-scale structures at the highest Prandtl number of 70 (§ 3.2), and examine the relevant spectra (§ 3.3). We finally discuss the generation mechanism of the vertically thin structures of the density fluctuations, modifying the theory for a passive scalar (Batchelor 1959) into a theory for a buoyant scalar (§ 3.4).

2. Numerical procedure

We consider the turbulent flow of a density-stratified fluid whose stratification is generated by a buoyant scalar of Prandtl number unity or larger ($Pr = \nu^*/\kappa^* \geqslant 1$). The quiescent fluid has the density distribution of $\bar{\rho}^*(z^*) = \rho_0^* + (\mathrm{d}\bar{\rho}^*/\mathrm{d}z^*)z^*$ (where z^* is the vertical coordinate and ρ_0^* is a representative density of the fluid) with a constant vertical density gradient $\mathrm{d}\bar{\rho}^*/\mathrm{d}z^* = \mathrm{const.} < 0$. The Brunt–Väisälä frequency is given by $N^* = \sqrt{-(g^*/\rho_0^*)(\mathrm{d}\bar{\rho}^*/\mathrm{d}z^*)}$, where g^* is the gravitational acceleration. As an initial condition for the decaying turbulence, we consider an isotropic velocity fluctuation with the integral length scale of L_0^* and the r.m.s. velocity of U_0^*.

The temporal variation of velocity, u_i^* ($i = 3$ denotes the vertical component), is governed by the Navier–Stokes equations under the Boussinesq approximation, i.e.

$$\frac{\partial u_i}{\partial t} + u_j \frac{\partial u_i}{\partial x_j} = -\frac{\partial p'}{\partial x_i} + \frac{1}{Re_0} \frac{\partial^2 u_i}{\partial x_j^2} - \frac{1}{Fr_0^2} \rho' \delta_{i3}, \qquad (2.1)$$

the density perturbation from its mean field ρ'^* ($= \rho^* - \bar{\rho}^*(x_3^*)$) is governed by the transport equation of density, i.e.

$$\frac{\partial \rho'}{\partial t} + u_j \frac{\partial \rho'}{\partial x_j} = \frac{1}{Re_0 Pr} \frac{\partial^2 \rho'}{\partial x_j^2} + u_3, \qquad (2.2)$$

and the incompressibility condition is given by

$$\frac{\partial u_i}{\partial x_i} = 0. \qquad (2.3)$$

Hereafter, (u, v, w) and (x, y, z) are read as (u_1, u_2, u_3) and (x_1, x_2, x_3), respectively, and the quantities without an asterisk denote the values non-dimensionalised by the length scale L_0^*, the velocity scale U_0^*, the pressure scale $\rho_0^* U_0^{*2}$ and the density scale $-L_0^* \, \mathrm{d}\bar{\rho}^*/\mathrm{d}z^*$. Throughout this study, the initial Reynolds number and the initial Froude number are fixed at $Re_0 = U_0^* L_0^*/\nu^* = 100$ and $Fr_0 = U_0^*/(N^* L_0^*) = 1$, and we examine the Prandtl-number dependence of the flow using three Prandtl numbers ($Pr = 1, 7$ and 70).

In this study, only the kinetic energy is assumed to exist initially, since there would be no initial potential energy due to density perturbations in the grid-generated stratified turbulence (e.g. Stillinger *et al.* 1983; Lienhard & Van Atta 1990). The initial energy spectrum is given in dimensional form by

$$E_K^*(k^*) = 16\sqrt{\frac{2}{\pi}} U_0^{*2} \frac{k^{*4}}{k_0^{*5}} \exp\left\{-2\left(\frac{k^*}{k_0^*}\right)^2\right\}. \qquad (2.4)$$

This corresponds to the final period of decay of isotropic turbulence (Orszag & Patterson 1972; Townsend 1976), and has been used for the initially isotropic stratified

Pr	Re_0	Fr_0	Time	Number of grid points	k_{max}	$\min[k_{max}/k_B]$
1	100	1	$0 \leqslant t \leqslant 40$	1024^3	170.5	6.47
7	100	1	$0 \leqslant t \leqslant 40$	1024^3	170.5	2.45
70	100	1	$0 \leqslant t \leqslant 6$	2048^3	341	1.55
70	100	1	$6 \leqslant t \leqslant 40$	1024^3	170.5	1.60

TABLE 1. List of parameters used for the present DNS. The minimum value of k_{max}/k_B appears initially (figure 7a), i.e. when the Batchelor wavenumber k_B is largest.

turbulence (e.g. Staquet & Godeferd 1998). Integration of the spectrum in the whole range of wavenumber k^* gives the initial kinetic energy $KE_0^* = 3U_0^{*2}/2$ and the initial integral scale L_0^* as

$$L_0^* = \frac{3\pi}{4KE_0^*} \int_0^\infty \frac{E_K^*(k^*)}{k^*} \, dk^* = \frac{\sqrt{2\pi}}{k_0^*}. \qquad (2.5)$$

We note that the statistical quantities shown in the following section are not very sensitive to the form of the initial energy spectrum, as long as the initial r.m.s. velocity and integral scale are the same.

In the actual numerical simulation, isotropic fluctuations satisfying (2.4) are developed in time without stratification until the enstrophy reaches its maximum, so that an isotropic turbulence is well developed. We then apply the undisturbed vertical density gradient, and set the time at $t = 0$. The simulation is terminated at $t = U_0^* t^*/L_0^* = 40$, which is equal to approximately six Brunt–Väisälä periods (the non-dimensional Brunt–Väisälä period is $T_{BV} = 2\pi U_0^*/(N^* L_0^*) = 2\pi Fr_0 \sim 6.3$). The microscale Reynolds number at $t = 0$ is $Re_\lambda = 42$. The k^{-1} spectrum for passive scalars has been observed in stationary turbulence at such a low Reynolds number (e.g. $Re_\lambda = 38$ in Yeung *et al.* (2002); $Re_\lambda = 8$ in Yeung *et al.* (2004)).

The vorticity equation obtained by taking the curl of (2.1) and the transport equation of the density perturbation (2.2) are solved by the Fourier spectral method in a cube with boundary conditions of period 4π in all directions. The nonlinear terms are evaluated pseudospectrally and the aliasing errors are removed by the $3/2$ rule, so that the maximum wavenumber k_{max} is 341 (and the minimum wavenumber k_{min} is 0.5) when 2048^3 grid points are used. The parameters used for the numerical simulations are summarised in table 1. For all cases, the value of k_{max}/k_B is always larger than 1.55, so that phenomena down to the Batchelor scale could be resolved. For the case with the highest Prandtl number ($Pr = 70$), we begin the simulation at $t = 0$ with 2048^3 grid points, and reduce the resolution to 1024^3 at $t = 6$. The decrease of grid resolution at $t = 6$ does not affect the numerical results since the Batchelor scale is well resolved ($k_{max}/k_B = 1.60$) even with the coarser grid (cf. figure 7a). For the time integration, the diffusive terms are calculated analytically using the integrating factor, while the other terms are approximated by the fourth-order Runge–Kutta method (Rogallo 1977).

The numerical code is parallelised using the message passing interface (MPI) based on the one-dimensional decomposition (i.e. decomposing the computational domain into slabs). The computations have been carried out on the NEC SX-ACE in the Cyberscience Center of Tohoku University, and the Earth Simulator Center of the Japan Agency of Marine-Earth Science and Technology. The execution time required

for the case of $Pr = 70$ is 19.2 h for the initial period of $0 \leqslant t \leqslant 6$ (with 256 nodes), and 21.8 h for the latter period of $6 \leqslant t \leqslant 40$ (with 64 nodes). The execution time is shorter for $Pr = 1$ and 7, i.e. 25.6 h for the whole period of $0 \leqslant t \leqslant 40$, using 64 nodes throughout the computation.

3. Results

3.1. *Energetics*

We first consider the time development of the kinetic energy $KE = \overline{u_i^2}/2$ and the potential energy $PE = \overline{\rho'^2}/(2Fr_0^2)$, where the overline denotes the spatial average over the entire periodic domain, i.e. $\overline{\cdot} = (1/(4\pi)^3)\int \cdot \, \mathrm{d}V$. Their decay rates, $\mathrm{d}KE/\mathrm{d}t$ and $\mathrm{d}PE/\mathrm{d}t$, are determined by the following equations (e.g. Gerz & Yamazaki 1993):

$$\frac{\mathrm{d}}{\mathrm{d}t}KE = -\frac{\overline{\rho'w}}{Fr_0^2} - \epsilon_K, \qquad (3.1)$$

$$\frac{\mathrm{d}}{\mathrm{d}t}PE = \frac{\overline{\rho'w}}{Fr_0^2} - \epsilon_P, \qquad (3.2)$$

where the kinetic and potential-energy dissipation rates are defined by $\epsilon_K = \overline{(\partial u_i/\partial x_j)^2}/Re_0$ and $\epsilon_P = \overline{(\partial \rho'/\partial x_j)^2}/(Pr\,Re_0Fr_0^2)$, respectively. The first term on the right-hand side of these equations, i.e. $\overline{\rho'w}/Fr_0^2$, is the vertical density flux which is responsible for the energy exchange between KE and PE.

Figure 2(*a*) indeed shows the initial decrease of KE and the initial increase of PE. After that, both energies show decaying oscillation with approximately half the Brunt–Väisälä period ($T_{BV}/2 = \pi Fr_0 = \pi$). The phases of oscillation are opposite since energy conversion between KE and PE continues. The kinetic energy KE can be decomposed into the horizontal kinetic energy $KE_H = \overline{u^2 + v^2}/2$ and the vertical kinetic energy $KE_V = \overline{w^2}/2$ (figure 2*b*), and only KE_V shows a clear oscillation while KE_H decays almost monotonically, since PE exchanges energy directly with KE_V.

Time oscillation of the vertical density flux is shown in figure 3(*a*), and comparison with figures 2(*a*) and 2(*b*) show that KE_V decreases and PE increases during $0 < t \lesssim 2$, i.e. when the vertical density flux is positive, while the opposite happens during $2 \lesssim t \lesssim 3$, i.e. when the vertical density flux is negative. This shows clearly that the energy exchange occurs through the vertical density flux (e.g. Gerz & Yamazaki 1993).

Now we consider the effect of the Prandtl number. According to (3.2), the initial growth of PE ($0.5 \lesssim t \lesssim 2$) is more significant for higher Prandtl numbers, since the dissipation rate ϵ_P is smaller (figure 3*b*) while the difference in the vertical density flux is small (figure 3*a*). Since the peak value of PE is larger, more energy can be converted back into KE_V during $2 \lesssim t \lesssim 3$, through the counter-gradient vertical density flux (figure 3*a*). This leads to a slightly larger KE_V and KE, during the same period (insets of figure 2*a*,*b*). The total energy ($TE = KE + PE$) also decays more slowly for a higher Prandtl number (results not shown), mainly because of the smaller ϵ_P.

We note that the difference of KE_V (and KE) between $Pr = 7$ and 70 is much smaller than the difference between $Pr = 1$ and 7. Indeed, as will be shown later in figure 13, the kinetic-energy spectra for $Pr = 7$ and 70 are almost identical at scales larger than the Kolmogorov scale, and the Prandtl-number effects appear only at scales smaller than the Kolmogorov scale. The velocity fluctuations at such small scales do not practically contribute to kinetic energy, so that the kinetic energy becomes insensitive to the large Prandtl numbers ($Pr = 7$ and 70). This may suggest that the
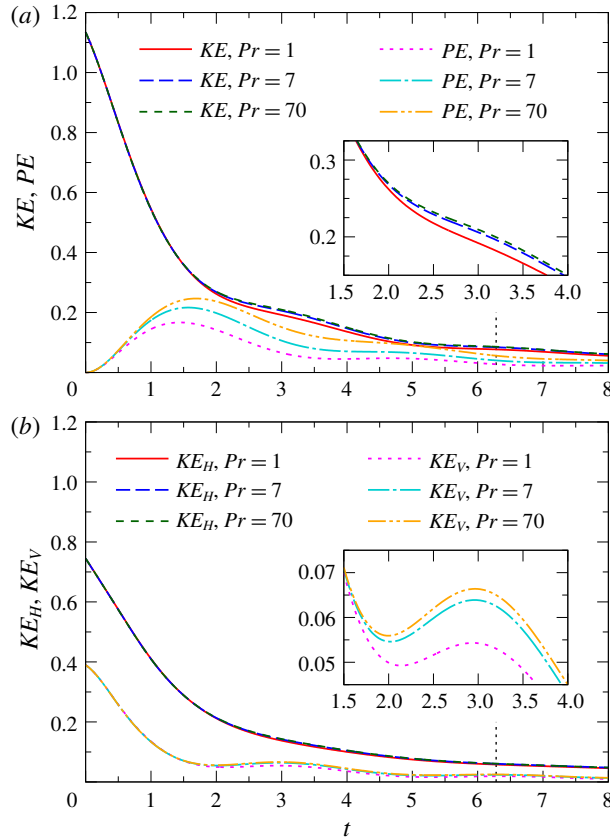
FIGURE 2. (Colour online) Temporal variations of (*a*) kinetic energy $KE = \overline{u_i^2}/2$ and potential energy $PE = \overline{\rho'^2}/(2Fr_0^2)$, and (*b*) horizontal kinetic energy $KE_H = \overline{u^2 + v^2}/2$ and vertical kinetic energy $KE_V = \overline{w^2}/2$. The insets in panels 2(*a*) and (*b*) are close-ups of KE and KE_V, respectively. The vertical dotted line indicates the Brunt–Väisälä period, i.e. $t = T_{BV} = 2\pi Fr_0 \; (= 6.28)$.

kinetic energy does not increase further even if we adopt a higher Prandtl number of $O(10^3)$, which is the typical Schmidt number for the scalar diffusion in liquids.

Figure 3(*a*) presents the Prandtl-number dependence of the vertical density flux. It is almost independent of *Pr* until it reaches the first peak at $t \sim 0.6$, but the *Pr* dependence appears at $t \sim 1.5$, after which the effects of density diffusion become significant. The vertical density flux becomes more negative and more counter-gradient for a higher Prandtl number (cf. figure 14*a*), in agreement with previous studies. For example, wind tunnel experiments using thermally stratified air ($Pr = 0.7$) show only a weak counter-gradient flux (Lienhard & Van Atta 1990), while the water channel experiments using salinity stratification ($Pr = 700$) show a stronger counter-gradient flux (Komori & Nagata 1996). The Prandtl-number dependence of the counter-gradient flux was predicted also by the rapid distortion theory as an effect of molecular diffusion (Hanazaki & Hunt 1996).

The dissipation rates of *KE* and *PE*, i.e. ϵ_K and ϵ_P, decrease almost monotonically (figure 3*b*) after $t \sim 3$, since the temporal oscillation occurs only at large scales,
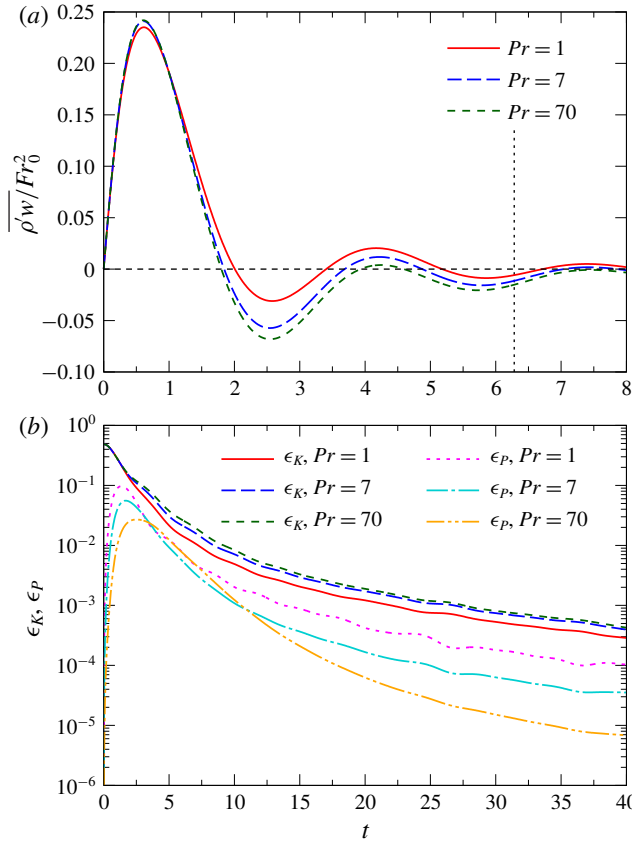
FIGURE 3. (Colour online) Temporal variations of (*a*) vertical density flux $\overline{\rho'w}/Fr_0^2$ and (*b*) kinetic- and potential-energy dissipation rates $\epsilon_K = \overline{(\partial u_i/\partial x_j)^2}/Re_0$ and $\epsilon_P = \overline{(\partial \rho'/\partial x_j)^2}/(Pr\,Re_0 Fr_0^2)$. The vertical dotted line in panel (*a*) indicates the Brunt–Väisälä period $t = T_{BV} = 2\pi Fr_0$ ($= 6.28$).

while the dissipation is dominated by the non-oscillating small-scale components. The kinetic-energy dissipation rate ϵ_K is slightly larger for a higher Prandtl number ($Pr > 1$), since the potential energy at scales smaller than the Kolmogorov scale becomes larger (cf. figure 13) and more energy is converted into kinetic energy at small scales through the vertical density flux.

On the other hand, the potential-energy dissipation rate ϵ_P is smaller for a larger Prandtl number due to the smaller diffusion coefficient. The time at which ϵ_P reaches its maximum is delayed since it takes a longer time for a high-Prandtl-number scalar to transfer potential energy to its small Batchelor scale and complete the initial cascading process of the potential energy.

Figure 4 shows the temporal variation of the correlation coefficient of the vertical density flux defined by $\overline{\rho'w}/(\rho'_{rms}w_{rms})$, in which $\rho'_{rms} = (\overline{\rho'^2})^{1/2}$ and $w_{rms} = (\overline{w^2})^{1/2}$. The time is non-dimensionalised here by the Brunt–Väisälä period $T_{BV}^* = 2\pi/N^*$, and we note that the correlation coefficient is initially equal to unity when the initial density fluctuation is absent, and oscillates at approximately half the Brunt–Väisälä period (e.g. Gerz & Yamazaki 1993; Hanazaki & Hunt 1996). The Prandtl-number effect is
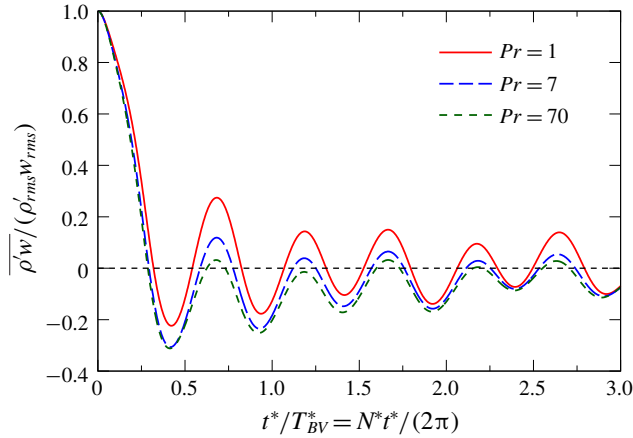
FIGURE 4. (Colour online) Correlation coefficient of the vertical density flux $\overline{\rho'w}/(\rho'_{rms}w_{rms})$ plotted against the buoyancy time t^*/T^*_{BV}.

initially small until the correlation coefficient first becomes zero ($N^*t^*/(2\pi) \lesssim 0.3$), but it becomes apparent with time, and the flux is persistently more strongly counter-gradient for larger Prandtl numbers (Hanazaki & Hunt 1996; Komori & Nagata 1996).

The decay rate of *KE* and *PE* is examined by replotting figure 2(*a*) in a double-logarithmic chart (figure 5). The kinetic energy decays like $\sim t^{-1.1}$ after $t \sim 2$, independent of *Pr*. We note that the numerical simulation by Staquet & Godeferd (1998) shows a decay exponent of ~ -1.0, and the experiments show a decay exponent of ~ -1.3 (Lienhard & Van Atta 1990; Fincham *et al.* 1996; Praud *et al.* 2005). Since the experiments for a homogeneous fluid also give a similar decay exponent of -1.3 to -1.0, the above results for stratified fluids show that the stratification has only small effects on the decay rate of *KE* (i.e. $\mathrm{d}KE/\mathrm{d}t$). For a higher Prandtl number, the vertical density flux $\overline{\rho'w}/Fr_0^2$ becomes more counter-gradient near the Kolmogorov scale (figure 14*a*) and injects more energy into the vertical velocity component. Then, the kinetic energy becomes larger at small scales (figure 13), and ϵ_K increases (figure 3*b*). These two effects approximately cancel on the right-hand side of (3.1), so that the decay rate of *KE* is rather insensitive to the Prandtl number. On the other hand, the potential energy decays faster for a larger Prandtl number for a certain period ($2 \lesssim t \lesssim 10$) after the *PE* becomes maximum. After that moment, however, *PE* decays like $\sim t^{-1.1}$ regardless of *Pr*, since the decrease of ϵ_P with increasing *Pr* cancels the decrease of $\overline{\rho'w}/Fr_0^2$ on the right-hand side of (3.2). Thus, the ratio *PE/KE* remains approximately constant at large times ($t \gtrsim 10$).

We next examine how the anisotropy develops in the large-scale motion. Figure 6 shows the temporal evolution of $KE_H/(2KE_V) = \overline{u^2 + v^2}/(2\overline{w^2})$, which should become unity when the flow is isotropic. The ratio actually exceeds unity, and the overall value increases until $t \sim 15$, indicating that the vertical motion is suppressed by buoyancy, and the horizontal flow becomes more dominant. When $Pr = 1$, the ratio fluctuates around 2.2 after $t \sim 15$, in agreement with Godeferd & Staquet (2003), who reported that the ratio of r.m.s. horizontal velocity to r.m.s. vertical velocity, i.e. $(KE_H/(2KE_V))^{1/2}$, approaches 1.5. The ratio $KE_H/(2KE_V)$ becomes smaller for a higher Prandtl number, since more potential energy is converted into vertical kinetic energy via the vertical density flux (figure 3*a*), and the increase of KE_V with *Pr* is
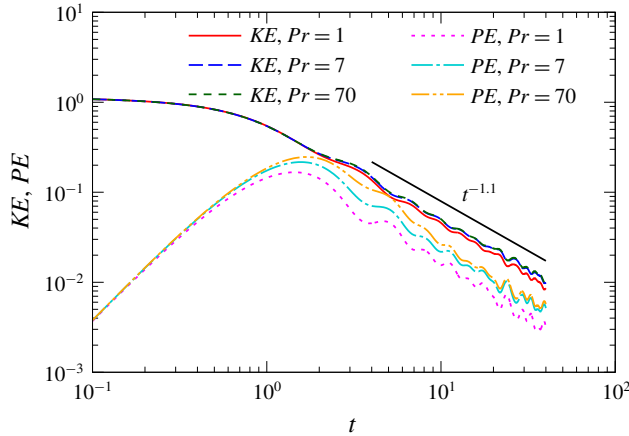
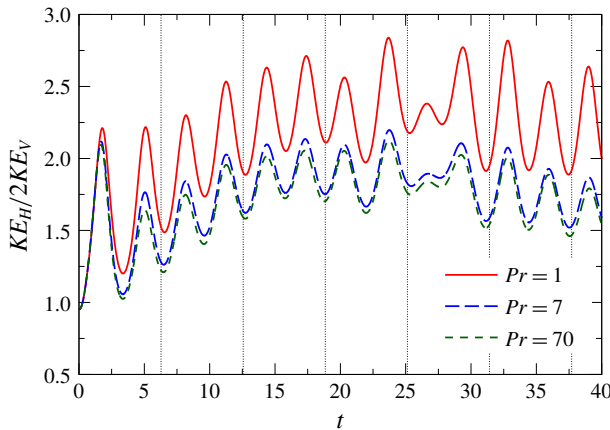FIGURE 5. (Colour online) Replot of figure 2(*a*) in a double-logarithmic chart.

FIGURE 6. (Colour online) Temporal variation of the energy ratio $KE_H/(2KE_V)$, which should be unity for isotropic turbulence. The vertical dotted lines indicate the time $t = nT_{BV}$ ($n = 1, 2, \ldots$), where T_{BV} ($= 2\pi Fr_0 = 6.28$) is the Brunt–Väisälä period.

larger than the increase of KE_H (figure 2*b*). However, the decrease of the ratio due to the increasing Pr seems to saturate between $Pr = 7$ and $Pr = 70$ for the same reason as explained earlier in figure 2.

The temporal developments of the Kolmogorov wavenumber $k_K^* = (\epsilon_K^*/\nu^{*3})^{1/4}$, the Ozmidov wavenumber $k_O^* = (N^{*3}/\epsilon_K^*)^{1/2}$ and the Batchelor wavenumber $k_B^* = Pr^{1/2}k_K^*$ for $Pr = 70$ are plotted in figure 7(*a*) in their non-dimensional forms (i.e. $k_K = k_K^* L_0^*$, $k_O = k_O^* L_0^*$ and $k_B = k_B^* L_0^*$). The Ozmidov wavenumber determines the minimum size of turbulent eddies whose overturning motion is prohibited by buoyancy (Dougherty 1961; Ozmidov 1965). It increases as ϵ_K decreases with time. On the other hand, the Kolmogorov wavenumber decreases with time, and agrees with the Ozmidov wavenumber at $t \sim 8$. The agreement occurs always at the same wavenumber, i.e. at $k_P^* = (N^*/\nu^*)^{1/2}$. We call k_P^* the primitive wavenumber since the corresponding length has been called the primitive length scale in stratified turbulence (Barry *et al.* 2001). The primitive wavenumber k_P^*, by its definition, is always between k_K^* and k_O^*. In the
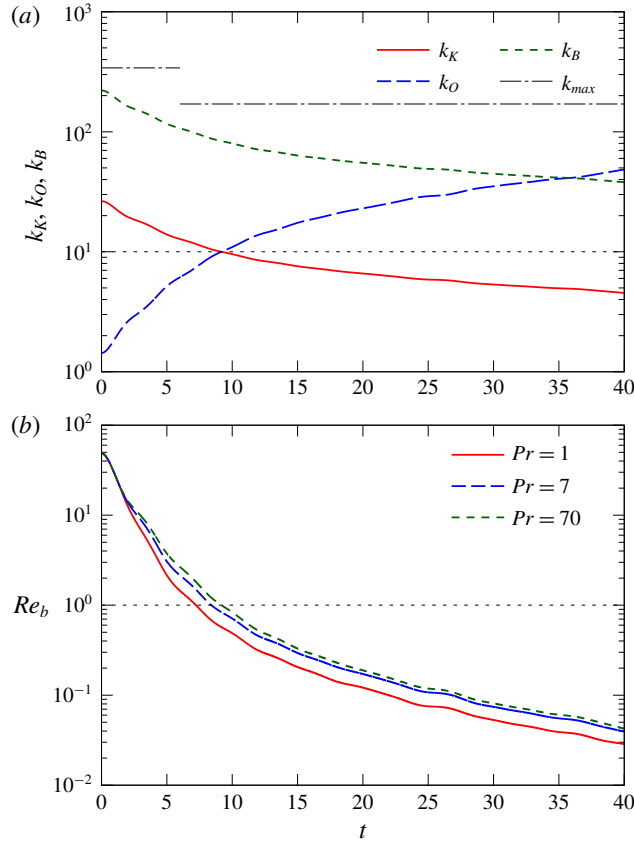
FIGURE 7. (Colour online) The evolution of (*a*) Kolmogorov, Ozmidov and Batchelor wavenumbers k_K, k_O and k_B for $Pr = 70$, and (*b*) buoyancy Reynolds number Re_b for $Pr = 1$, 7 and 70. In panel (*a*), the two horizontal dash-dotted lines indicate the maximum wavenumbers (k_{max}) resolved by the two grids used for the computation ($k_{max} = 341$ when $t \leqslant 6$, and $k_{max} = 170.5$ when $6 \leqslant t \leqslant 40$), and the horizontal dotted line indicates the primitive wavenumber ($k_P = 10$).

present numerical simulation, its non-dimensional value $k_P = (Re_0/Fr_0)^{1/2}$ ($= 10$) is invariant, since Re_0 ($= 100$) and Fr_0 ($= 1$) are fixed. The agreement time between k_K and k_O is slightly delayed as the Prandtl number becomes larger. This can be inferred from figure 3(*b*), which shows the increase of ϵ_K with Pr, and hence the increase of k_K and the decrease of k_O, although the results for $Pr = 1$ and 7 are not included in figure 7(*a*).

We present in figure 7(*b*) the temporal variation of the buoyancy Reynolds number

$$Re_b = \frac{\epsilon_K^*}{\nu^* N^{*2}} = \left(\frac{k_K^*}{k_O^*}\right)^{4/3}, \tag{3.3}$$

determined by the ratio between the Ozmidov scale and the Kolmogorov scale. If the buoyancy Reynolds number is larger than unity ($k_K > k_O$), the smallest eddy is not affected by buoyancy, and the flow at the Kolmogorov scale would be isotropic. The buoyancy Reynolds number starts at approximately 50 in our simulation, and
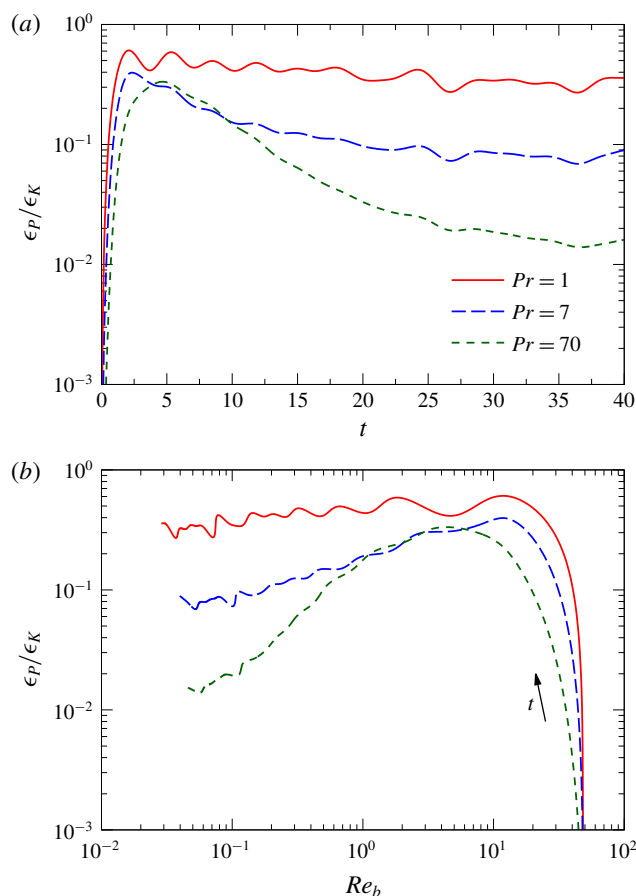
FIGURE 8. (Colour online) (*a*) Temporal variation of the mixing coefficient ϵ_P/ϵ_K. (*b*) Mixing coefficient as a function of the buoyancy Reynolds number Re_b, which decreases with time.

decreases monotonically with time. It decreases to unity at $t \sim 8$, i.e. when the decreasing k_K and the increasing k_O agree at k_P. After the buoyancy Reynolds number has decreased far below unity, most of the energy dissipates at large scales, and the flow is sometimes called viscosity-affected stratified flow (Brethouwer *et al.* 2007). The larger Prandtl number slows down the decrease of the buoyancy Reynolds number because more potential energy is converted into kinetic energy at small scales and retards the decrease of ϵ_K in (3.3).

Figure 8(*a*) shows the time development of the mixing coefficient ϵ_P/ϵ_K. It increases initially with the increase of ϵ_P (cf. figure 3*b*), but then decreases with some fluctuations. The mixing coefficient at $Pr = 1$ asymptotes to approximately 0.3, in agreement with the previous numerical simulations (Riley & de Bruyn Kops 2003). The value is also close to that of Maffioli *et al.* (2016) observed at much higher Reynolds numbers ($\sim 10^4$) and lower Froude numbers ($\lesssim 0.03$).

At early times ($t \sim 5$), the mixing coefficient does not depend strongly on the Prandtl number, but the decrease with time is more significant for higher Prandtl numbers. This occurs since ϵ_P becomes progressively smaller for higher Pr, while ϵ_K is always

comparable (figure 3*b*). As time proceeds ($t \gtrsim 10$), and when the buoyancy Reynolds number falls below unity, the contour surfaces of the density perturbation become flat (cf. figures 10*d*, 11*f* and 13*c*,*d*). Then, the horizontal diffusion becomes weak, and will reduce ϵ_P. Figure 8(*b*) indeed shows that the difference in ϵ_P/ϵ_K becomes conspicuous after Re_b becomes below unity. This may also explain why the decrease of the mixing coefficient due to Pr is more significant in the present simulation than in the mixing-layer simulation by Salehipour *et al.* (2015) where the buoyancy Reynolds number was much larger ($Re_b \gtrsim 10$).

3.2. *Spatial distributions of energy*

We next show in figure 9 the spatial distributions of the kinetic energy $u_i^2/2$ and the potential energy $\rho'^2/(2Fr_0^2)$ at $t = 4$, for low and high Prandtl numbers ($Pr = 1$ and 70). There is a strong effect of the Prandtl number on the potential energy, since Pr controls the cascading process of the scalar. In the case of $Pr = 70$, the potential-energy distribution (figure 9*d*) has a much smaller scale than that of the kinetic energy (figure 9*c*), since the Batchelor scale is much smaller than the Kolmogorov scale, while in the case of $Pr = 1$ (figures 9*a* and 9*b*), the length scales are comparable. On the other hand, the effect of Pr on the kinetic-energy distribution is small, and the results for $Pr = 1$ (figure 9*a*) and $Pr = 70$ (figure 9*c*) are similar. However, the isosurfaces at $Pr = 70$ have small undulations, which do not exist at $Pr = 1$. The undulations would be due to the energy converted from the potential energy at scales smaller than the Kolmogorov scale (cf. figure 14*a*).

At this early time ($t = 4$), the flow is only weakly affected by buoyancy since the time in units of the Brunt–Väisälä period is small ($t^*/T_{BV}^* = N^*t^*/(2\pi) = t/(2\pi Fr_0) \simeq 0.64 < 1$). For example, in the case of $Pr = 70$, the ratio k_K/k_O ($\simeq 4$, figure 7*a*) gives a rather large value of Re_b ($\simeq 6 > 1$, figure 7*b*), meaning that the stratification is effective only in the large-scale motion. Then, the kinetic-energy distribution looks nearly isotropic, and the scalar behaves like a passive scalar in isotropic turbulence (figures 9*c* and 9*d*). The large buoyancy Reynolds number Re_b (> 1) is maintained also for $Pr = 1$ (figure 7*b*). Therefore, both the kinetic- and potential-energy distributions appear approximately isotropic for both $Pr = 1$ and 70.

As time proceeds, the Ozmidov scale becomes smaller (figure 7*a*) and the buoyancy becomes dominant down to smaller scales, including the energy-containing scale. Then, the vertical kinetic energy becomes smaller than the horizontal kinetic energy, as observed in the previous experiments (e.g. Lienhard & Van Atta 1990), numerical simulations (e.g. Riley *et al.* 1981; Métais & Herring 1989) and in our figure 6. At a much later time ($t = 40$ or $t^*/T_{BV}^* = N^*t^*/(2\pi) \simeq 6.4 > 1$), the isosurfaces of the kinetic and potential energy have pancake structures that enclose much of the kinetic and potential energies, as shown in figure 10. Since the smaller-scale fluctuations observed when $t = 4$ (figure 9) have already decayed, only the large-scale structures remain. We note that the horizontal scales of isosurfaces are comparable in the kinetic- and potential-energy distributions, not only for $Pr = 1$ (figures 10*a* and 10*b*) but also for $Pr = 70$ (figures 10*c* and 10*d*). There are horizontal wrinkles on the surface of pancakes of potential energy at $Pr = 70$ (cf. figure 11*f*). These are the small-scale vertical structures observed only at high Prandtl numbers, not observed at lower Prandtl numbers (e.g. figure 10*b*). We will discuss the dominance of the vertically sheared horizontal flow later (cf. figures 17 and 18).

To observe the small-scale structures more clearly, the distributions of potential energy $\rho'^2/(2Fr_0^2)$ in the vertical plane ($y = 0$) are presented in colour scale in
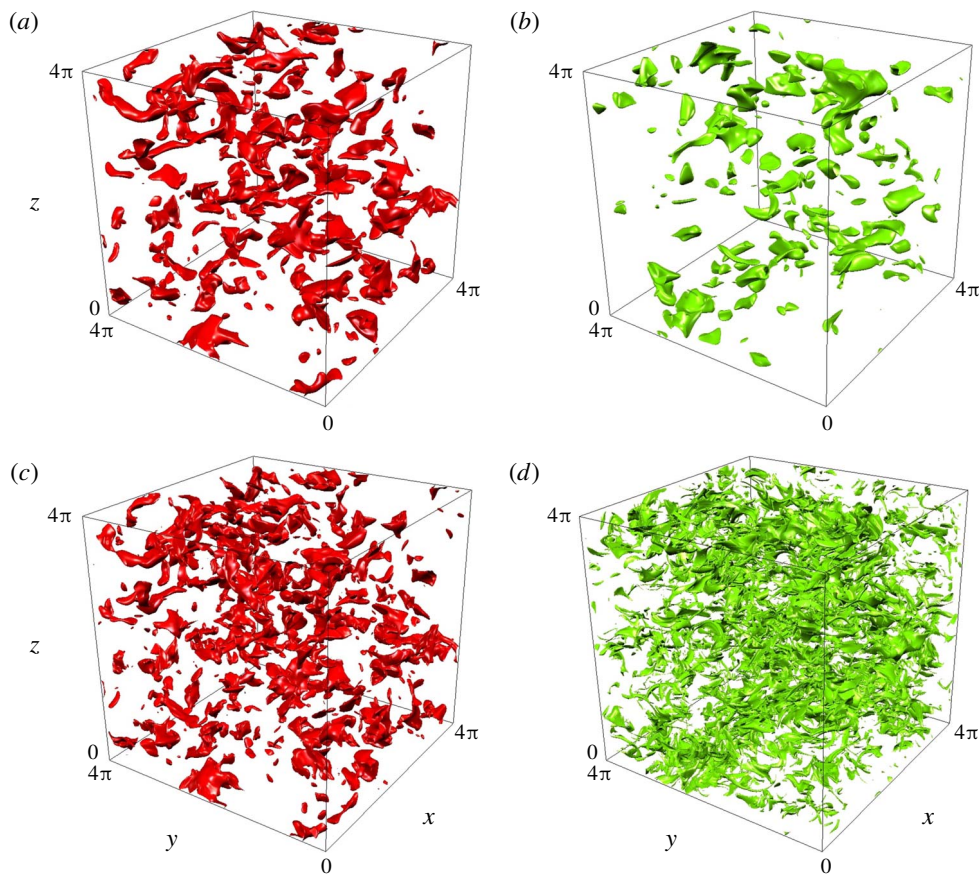
FIGURE 9. (Colour online) Spatial distributions of the energies at $t = 4$. The panels show the isosurfaces of: (*a*) kinetic energy $u_i^2/2$ ($= 3KE$) at $Pr = 1$; (*b*) potential energy $\rho'^2/(2Fr_0^2)$ ($= 6PE$) at $Pr = 1$; (*c*) kinetic energy $u_i^2/2$ ($= 3KE$) at $Pr = 70$; and (*d*) potential energy $\rho'^2/(2Fr_0^2)$ ($= 6PE$) at $Pr = 70$.

figure 11, again at $t = 4$ and 40. In agreement with figure 9, the potential-energy distribution at $t = 4$ is affected significantly by the Prandtl number, and the result for $Pr = 70$ (figure 11*e*) contains much finer structures than those for lower Prandtl numbers (figures 11*a* and 11*c*). The structures at $t = 40$ are rather independent of Pr (figures 11*b*, 11*d* and 11*f*) since most of the small-scale components below the Kolmogorov scale have decayed (cf. figures 13*c* and 13*d*). However, similar to the result at $t = 4$ (figure 11*e*), the vertical structure of the potential energy at high $Pr(= 70)$ has components of very small scales, which appear as many thin horizontal streaks in figure 11(*f*). These streaks correspond to the horizontal wrinkles on the surface of pancakes (figure 10*d*). These would be due to the high-vertical-wavenumber components observed in the potential-energy spectra, which will be discussed later (cf. figure 13*d*).

The agreement between the horizontal scales of the velocity and density perturbations at long time, observed even at a high Prandtl number ($Pr = 70$) in figure 10, is
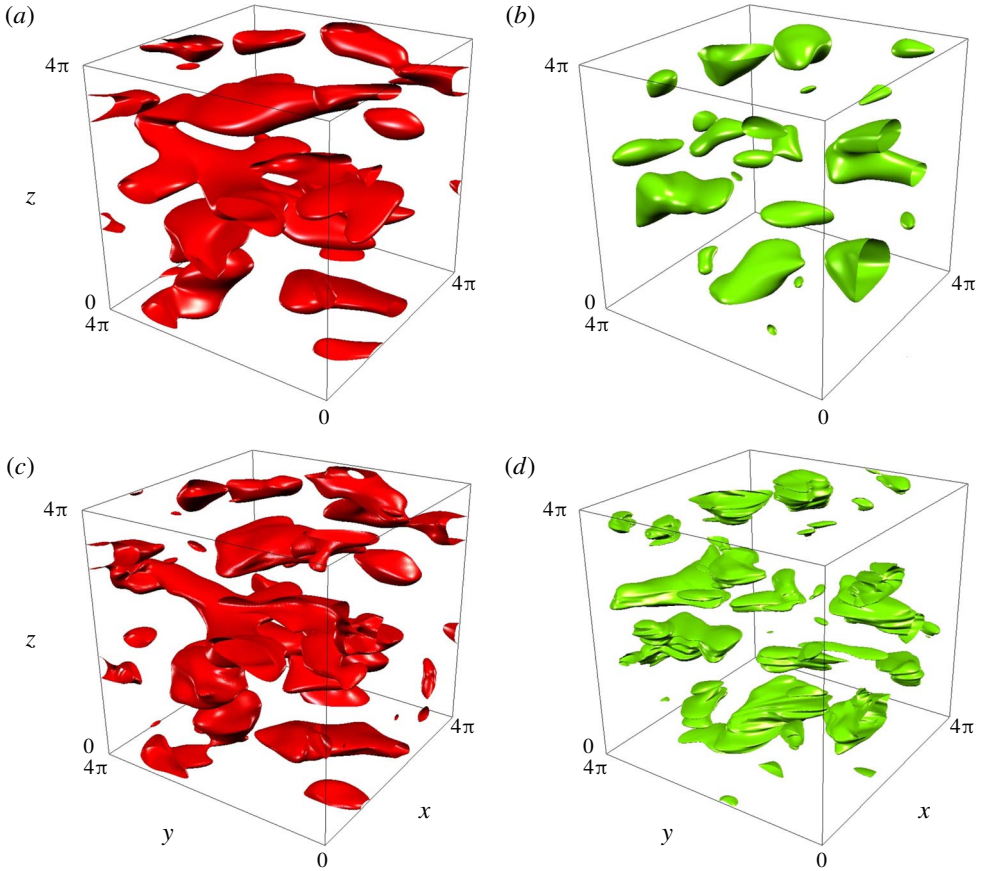
FIGURE 10. (Colour online) Spatial distributions of the energies at $t = 40$. The panels show the isosurfaces of: (*a*) kinetic energy $u_i^2/2$ ($= 2KE$) at $Pr = 1$; (*b*) potential energy $\rho'^2/(2Fr_0^2)$ ($= 4PE$) at $Pr = 1$; (*c*) kinetic energy $u_i^2/2$ ($= 2KE$) at $Pr = 70$; and (*d*) potential energy $\rho'^2/(2Fr_0^2)$ ($= 4PE$) at $Pr = 70$.

identified in figure 12 by the longitudinal Taylor microscales of velocity

$$\lambda_i^2 = \overline{u_i^2} \left/ \overline{\left(\frac{\partial u_i}{\partial x_i}\right)^2}\right., \quad (i = 1, 2, 3), \tag{3.4}$$

(no summation is taken over the repeated index *i*), and those of density perturbation

$$\lambda_{\rho',i}^2 = \overline{\rho'^2} \left/ \overline{\left(\frac{\partial \rho'}{\partial x_i}\right)^2}\right., \quad (i = 1, 2, 3), \tag{3.5}$$

where λ_1 and λ_3 are associated with the horizontal and vertical scales of velocity, and $\lambda_{\rho',1}$ and $\lambda_{\rho',3}$ are associated with those of density perturbations (e.g. Riley *et al.* 1981). The initial values of λ_1 and λ_3 are almost equal ($\lambda_1 = \lambda_3$) since the initial velocity fluctuations are isotropic. However, as time proceeds, the
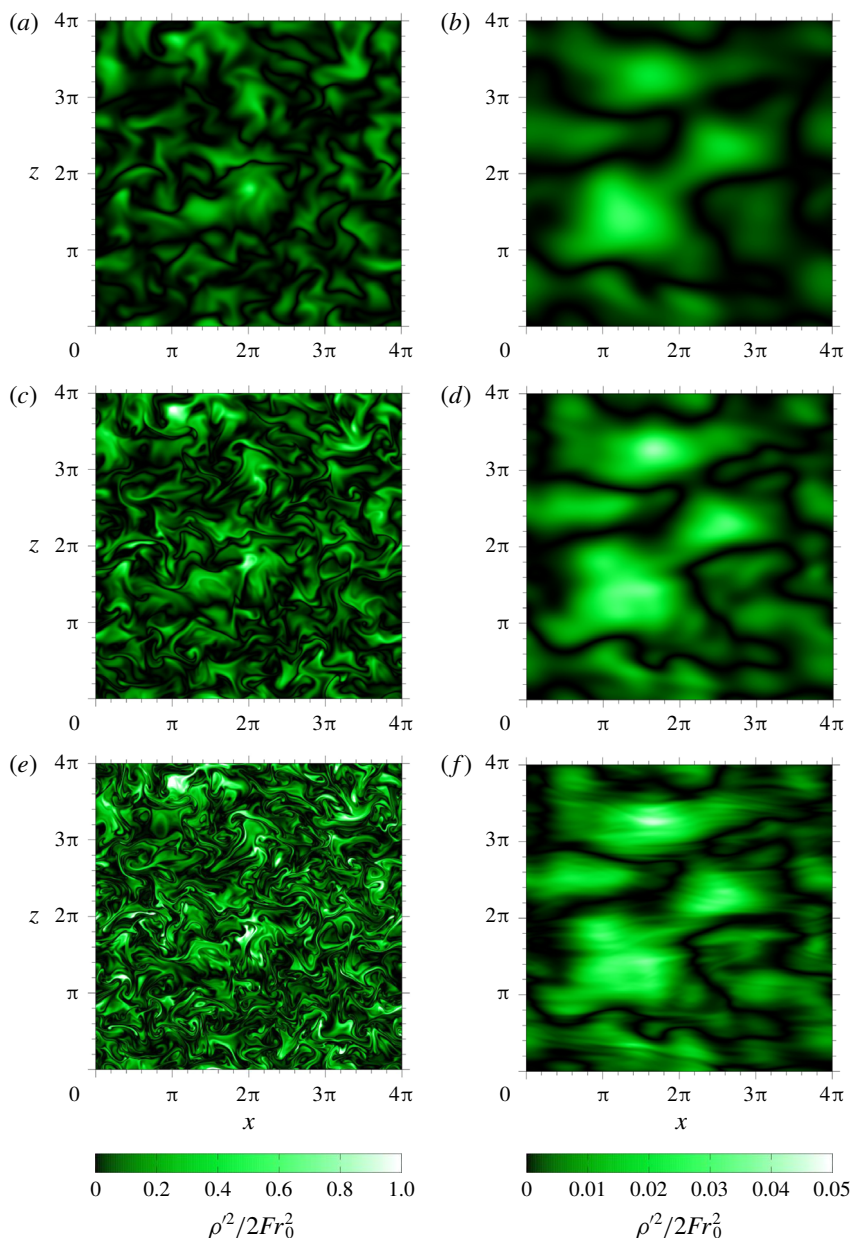
FIGURE 11. (Colour online) Spatial distributions of the potential energy $\rho'^2/(2Fr_0^2)$ in the vertical plane ($y = 0$). The panels show the colour-scale image at: (*a*) $Pr = 1$, $t = 4$; (*b*) $Pr = 1$, $t = 40$; (*c*) $Pr = 7$, $t = 4$; (*d*) $Pr = 7$, $t = 40$; (*e*) $Pr = 70$, $t = 4$; and (*f*) $Pr = 70$, $t = 40$.

horizontal microscales become larger than the vertical microscales ($\lambda_1 > \lambda_3$ and $\lambda_{\rho',1} > \lambda_{\rho',3}$), corresponding to the appearance of the pancake structure in the kinetic and potential-energy distributions (e.g. at $t = 40$, figure 10).

When $Pr = 1$ (figure 12*a*), the microscales of velocity are nearly equal to those of density perturbation at all times (i.e. $\lambda_1 \simeq \lambda_{\rho',1}$ and $\lambda_3 \simeq \lambda_{\rho',3}$). With the increase
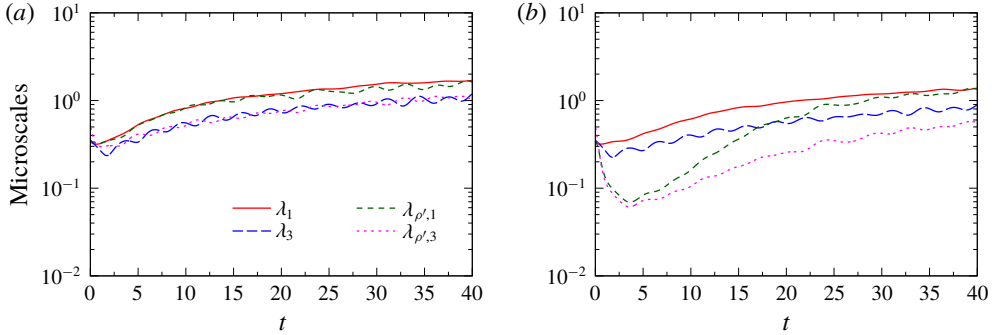
FIGURE 12. (Colour online) Temporal variation of the horizontal and vertical Taylor microscales of velocity and density perturbation for (*a*) $Pr = 1$ and (*b*) $Pr = 70$.

of Pr (= 70, figure 12*b*), however, the temporal behaviour of the microscales of density perturbation ($\lambda_{\rho',1}$ and $\lambda_{\rho',3}$) changes significantly, while that of the velocity microscales (λ_1 and λ_3) changes only a little. Namely, the microscales $\lambda_{\rho',1}$ and $\lambda_{\rho',3}$ initially decrease significantly due to the initial potential-energy cascade ($t \lesssim 4$), but after that, they increase again, and the horizontal microscale of density perturbation $\lambda_{\rho',1}$ becomes almost equal to the horizontal microscale of velocity λ_1 at large times ($t \gtrsim 30$). The increase of the vertical microscale $\lambda_{\rho',3}$ is not so large, and it is still smaller than the vertical microscale of velocity λ_3 at the end of the simulation ($t = 40$). These results are consistent with the agreement only in the horizontal scale of the kinetic- and potential-energy distributions at $Pr = 70$ (figure 10*c*,*d*).

3.3. *Energy spectra*

We next present the energy spectrum in order to further investigate the small-scale anisotropy of the high-Pr scalar distribution at late times. The horizontal and the vertical spectra of the kinetic energy are defined by

$$E_K(k_H) = \sum_{\substack{\left|\sqrt{k_x^2 + k_y^2} - k_H\right| < k_{min}/2 \\ k_z}} \frac{1}{2}|\hat{u}_i(k_x, k_y, k_z)|^2 \frac{1}{k_{min}} \tag{3.6}$$

and

$$E_K(k_V) = \sum_{\substack{|k_z| = k_V \\ k_x, k_y}} \frac{1}{2}|\hat{u}_i(k_x, k_y, k_z)|^2 \frac{1}{k_{min}}, \tag{3.7}$$

respectively. Here, $\hat{u}_i$ denotes the Fourier component of u_i, its argument (k_x, k_y, k_z) is the wavenumber vector, and the minimum wavenumber k_{min} is 0.5 since the side of the computational box is 4π in the non-dimensional form. Similarly, we define the horizontal and vertical potential-energy spectra as follows:

$$E_P(k_H) = \sum_{\substack{\left|\sqrt{k_x^2 + k_y^2} - k_H\right| < k_{min}/2 \\ k_z}} \frac{1}{2Fr_0^2}|\hat{\rho}'(k_x, k_y, k_z)|^2 \frac{1}{k_{min}}, \tag{3.8}$$

and

$$E_P(k_V) = \sum_{\substack{|k_z|=k_V \\ k_x,k_y}} \frac{1}{2Fr_0^2} |\hat{\rho}'(k_x, k_y, k_z)|^2 \frac{1}{k_{min}}. \tag{3.9}$$

The horizontal and vertical spectra of the kinetic and potential energy at $t = 4$ and $t = 40$ are plotted in figure 13 for all the Prandtl numbers.

At an early time of $t = 4$ (figure 13a,b), the Kolmogorov wavenumber is greater than the Ozmidov wavenumber (i.e. $Re_b > 1$) and the buoyancy does not affect the flow at the Kolmogorov scale. Indeed, the comparison between figures 13(a) and 13(b) shows that the isotropy of the velocity and density perturbations ($E_K(k_H) \sim E_K(k_V)$ and $E_P(k_H) \sim E_P(k_V)$ at the same k_H and k_V) still remains below the Kolmogorov scale. We note also that when $Pr = 1$, i.e. when the Kolmogorov scale and the Batchelor scale agree, the kinetic-energy spectra are almost equal to the potential-energy spectra at high wavenumbers (i.e. $E_K(k_H) = E_P(k_H)$ at $k_H \gtrsim k_K$ and $E_K(k_V) = E_P(k_V)$ at $k_V \gtrsim k_K$). The potential-energy spectra below the Kolmogorov scale are larger for a larger Prandtl number due to the scalar cascade to a smaller diffusion scale. The kinetic-energy spectra below the Kolmogorov scale also increase with the Prandtl number due to the larger energy conversion from the potential energy by the vertical density flux (cf. figures 3a,b and 14a). On the other hand, at large scales ($k < k_K$), the difference due to the Prandtl number is small in figure 13(a,b). The k^{-1} power law of the potential-energy spectrum appears at $Pr = 70$ for $k_K \lesssim k_H \lesssim k_B$ and $k_K \lesssim k_V \lesssim k_B$, showing that Batchelor's theory holds until the buoyancy affects the sub-Kolmogorov scale (i.e. when $k_O < k_K$). The $k_H^{-5/3}$ law of the energy spectra, which is observed by the recent high-Re simulations at $Pr = 1$ (e.g. Lindborg 2006; Brethouwer *et al.* 2007; Bartello & Tobias 2013; de Bruyn Kops 2015; Maffioli & Davidson 2016), is absent in the present result. This would be due to the low Reynolds number used in this study. The spectra will be observed if the Reynolds number becomes sufficiently large, since the low-wavenumber ($k < k_K$) spectra would not be affected significantly by the Prandtl number.

The energy spectra in the final period of decay ($t = 40$), i.e. when the Ozmidov wavenumber is far beyond the Kolmogorov wavenumber ($k_K \ll k_O$ or $Re_b \ll 1$, cf. figure 7), are presented in figure 13(c,d). In figure 13(c), the horizontal spectra of potential energy $E_P(k_H)$ for $Pr = 7$ and 70 decrease significantly at high wavenumbers, compared to the other spectra. These spectral curves approach the curves of kinetic-energy spectra $E_K(k_H)$ since the energy is converted from potential energy to kinetic energy via the vertical density flux. For example, when $Pr = 7$, the two spectral curves of $E_P(k_H)$ and $E_K(k_H)$ almost agree for $k_K < k_H \lesssim 10$. The tendency is weaker in the vertical spectra of potential energy $E_P(k_V)$ for $Pr = 7$ and 70 (figure 13d). This corresponds to the Prandtl-number dependence of the potential-energy distributions observed in figures 10 and 11, where the small-scale fluctuations in the vertical direction existed only in the case of $Pr = 70$ (figure 10d) and not in the case of $Pr = 1$ (figure 10b).

Figure 14(a) shows the Prandtl-number dependence of the co-spectrum of the vertical density flux

$$C_{\rho'w}(k) = \sum_{\left|\sqrt{k_x^2+k_y^2+k_z^2}-k\right|<k_{min}/2} \frac{1}{Fr_0^2} \text{Re}[\hat{\rho}'(k_x, k_y, k_z)\hat{w}^*(k_x, k_y, k_z)] \frac{1}{k_{min}}, \tag{3.10}$$
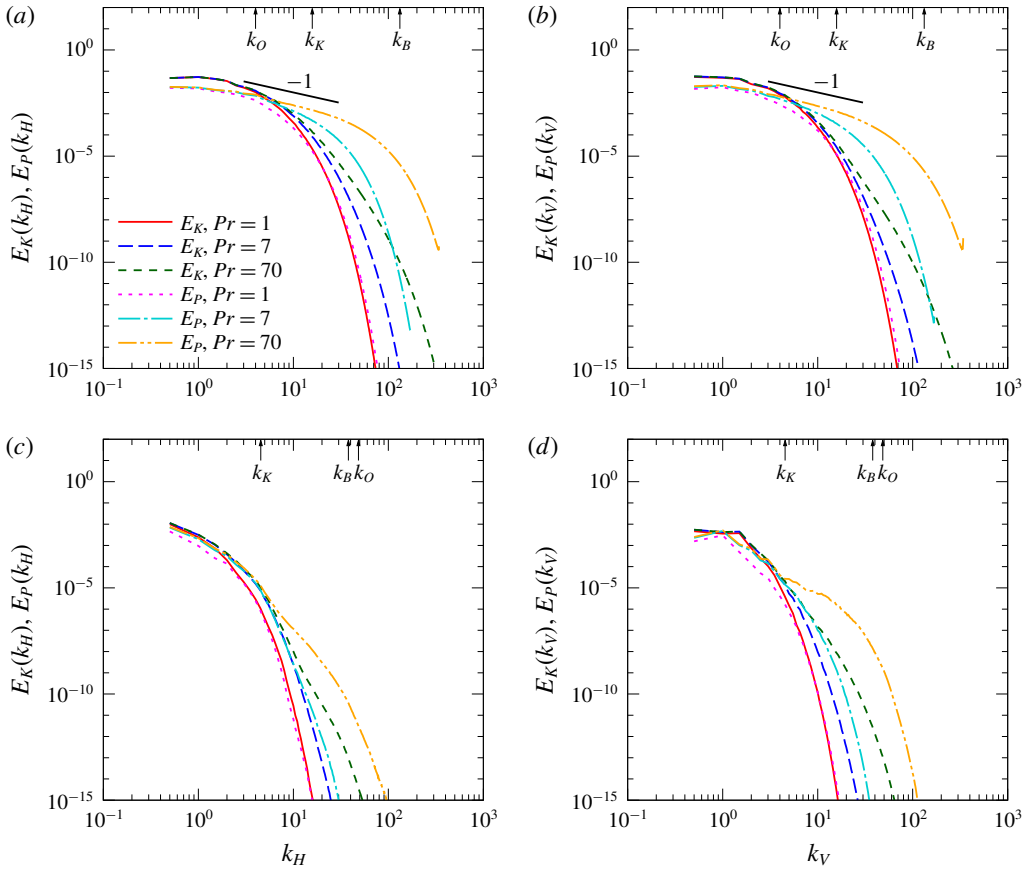
FIGURE 13. (Colour online) Plots of (*a*) $E_K(k_H)$ and $E_P(k_H)$ at $t = 4$, (*b*) $E_K(k_V)$ and $E_P(k_V)$ at $t = 4$, (*c*) $E_K(k_H)$ and $E_P(k_H)$ at $t = 40$ and (*d*) $E_K(k_V)$ and $E_P(k_V)$ at $t = 40$, where the four energy spectra $E_K(k_H)$, $E_K(k_V)$, $E_P(k_H)$ and $E_P(k_V)$ are defined by (3.6)–(3.9). The Kolmogorov, Ozmidov and Batchelor wavenumbers for $Pr = 70$ are indicated by the arrows at the top of each panel.

which satisfies

$$\frac{1}{Fr_0^2}\overline{\rho' w} = \int_0^\infty C_{\rho' w}(k)\, \mathrm{d}k, \qquad (3.11)$$

where the asterisk in (3.10) denotes the complex conjugate, and not a dimensional quantity. The co-spectrum at large scales ($k \lesssim k_O$) oscillates in time and changes sign, i.e. it is positive when $t = 4$ (figure 14*a*), while it is negative when $t = 6$. On the other hand, the co-spectrum at wavenumbers larger than the Kolmogorov wavenumber ($k \gtrsim k_K$) is persistently negative and counter-gradient, showing that the potential energy is converted continuously into kinetic energy.

   The larger potential energy in the small-scale fluctuations of a higher-Prandtl-number scalar would lead to a stronger counter-gradient flux at small scales, so that the vertical density flux $\overline{\rho' w}/Fr_0^2$ becomes more strongly counter-gradient (figure 3*a*). At the same time, the kinetic-energy spectra $E_K(k_H)$ and $E_K(k_V)$ decay more slowly near the Kolmogorov wavenumber (figure 13*a*,*b*).
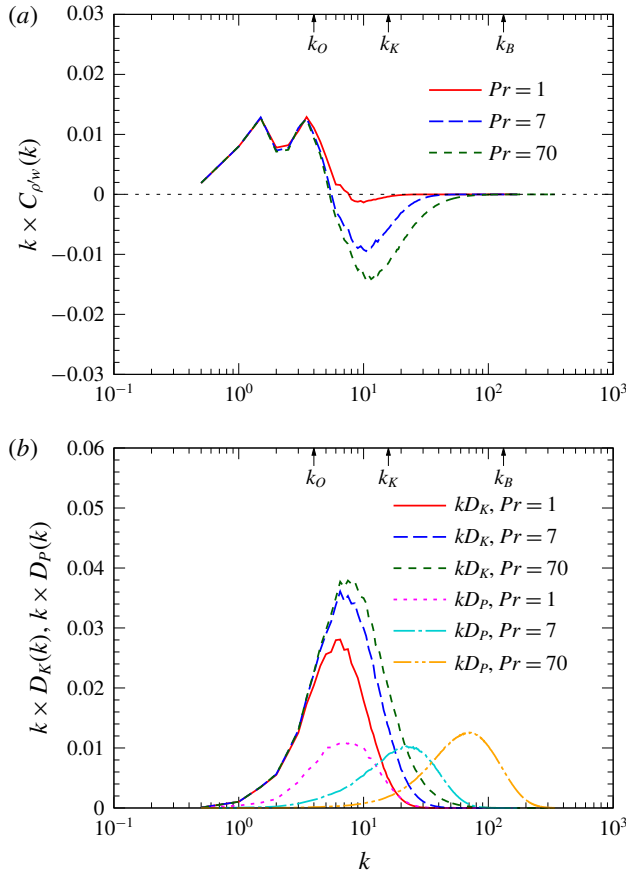
FIGURE 14. (Colour online) Prandtl-number dependence of (*a*) the co-spectrum of the vertical density flux, $C_{\rho'w}(k)$, and (*b*) dissipation spectra of kinetic and potential energies, $D_K(k)$ and $D_P(k)$, in the pre-multiplied form at $t = 4$. The Kolmogorov, Ozmidov and Batchelor wavenumbers for $Pr = 70$ are indicated by the arrows at the top of each panel.

The same spectral behaviour has been observed in the previous experiments. For example, water channel experiments for salt stratification ($Pr = 700$; Komori & Nagata 1996) showed a strong counter-gradient flux at high wavenumbers. On the other hand, wind tunnel experiments for thermally stratified flow ($Pr = 0.7$; Lienhard & Van Atta 1990) showed a weaker counter-gradient flux at low wavenumbers. In a numerical simulation for two Prandtl numbers ($Pr = 1$ and 2), Gerz & Yamazaki (1993) found a persistent counter-gradient flux at high wavenumbers only for $Pr = 2$. Similar Prandtl-number dependence has been obtained by the rapid distortion theory (RDT) (Hanazaki & Hunt 1996).

In figure 14(*b*) we show the pre-multiplied spectra of energy dissipation rates at $t = 4$. The dissipation spectra of kinetic energy and potential energy are defined by

$$D_K(k) = \sum_{\left|\sqrt{k_x^2+k_y^2+k_z^2}-k\right|<k_{min}/2} \frac{k_j^2}{Re_0}|\hat{u}_i(k_x, k_y, k_z)|^2 \frac{1}{k_{min}}, \tag{3.12}$$
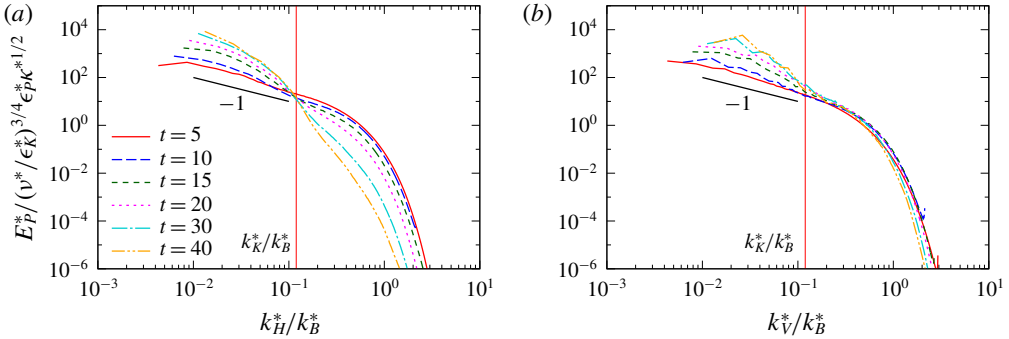
FIGURE 15. (Colour online) Normalised potential-energy spectrum for $Pr = 70$: (*a*) horizontal spectrum and (*b*) vertical spectrum. The vertical solid line shows the Kolmogorov wavenumber divided by the Batchelor wavenumber, i.e. $k_K^*/k_B^* = 1/\sqrt{70} \simeq 0.12$.

and

$$D_P(k) = \sum_{\left| \sqrt{k_x^2 + k_y^2 + k_z^2} - k \right| < k_{min}/2} \frac{k_j^2}{Pr\,Re_0 Fr_0^2} |\hat{\rho}'(k_x, k_y, k_z)|^2 \frac{1}{k_{min}}, \qquad (3.13)$$

respectively. The peak wavenumber of kinetic-energy dissipation ($kD_K(k)$) shifts only slightly with Pr, while that of potential-energy dissipation ($kD_P(k)$) increases significantly with Pr. Figure 14(*b*) shows also that the peak wavenumber of $kD_K(k)$ is close to the Kolmogorov wavenumber k_K, and the peak of $kD_P(k)$ is close to the Batchelor wavenumber k_B. The increase of the maximum value of $kD_K(k)$ with Pr explains the slight increase of ϵ_K as already discussed in figure 3(*b*). A similar trend has been observed in the vorticity spectrum of the turbulent mixing layer (see figures 12 and 13 of Salehipour *et al.* (2015)).

We now examine whether the energy spectra obey the well-known scaling laws. The potential-energy spectra normalised by the strain rate at the Kolmogorov scale $(\nu^*/\epsilon_K^*)^{1/2}$, the potential-energy dissipation rate ϵ_P^* and the scalar diffusion coefficient κ^* for $Pr = 70$ are shown in figure 15. Note that the Kolmogorov wavenumber normalised by the Batchelor wavenumber is constant in time: $k_K^*/k_B^* = 1/\sqrt{70} \simeq 0.12$. When $t \lesssim 10$, the spectral collapse onto a single curve at wavenumbers higher than the Batchelor wavenumber and the k^{-1} power law are clearly found in both the horizontal and the vertical spectra as well as the passive scalar spectrum (e.g. Bogucki *et al.* 1997; Yeung *et al.* 2004). After $t \sim 10$, at which the Ozmidov wavenumber exceeds the Kolmogorov wavenumber, the horizontal spectrum begins to decrease in $k_H^* > k_K^*$ and increase in $k_H^* < k_K^*$, resulting in a very steep spectrum. On the other hand, the Batchelor scaling reasonably holds for the vertical spectrum even after the Ozmidov wavenumber exceeds the Kolmogorov wavenumber ($t \gtrsim 10$); they converge well in $k_V^* > k_K^*$ as shown in figure 15(*b*). It is also found that the slope around $k_V^*/k_B^* \simeq 5 \times 10^{-2}$ becomes steeper as time passes, and eventually approaches -3.

Figure 16 presents the kinetic-energy spectra for $Pr = 70$ normalised by the energy dissipation ϵ_K^* and the kinematic viscosity ν^*. The result is similar to the normalised potential-energy spectrum in the sense that the horizontal spectrum deviates from the Kolmogorov scaling when $t \gtrsim 10$, whereas the vertical spectrum completely collapses onto a single curve. The collapse of the vertical spectrum is also reported
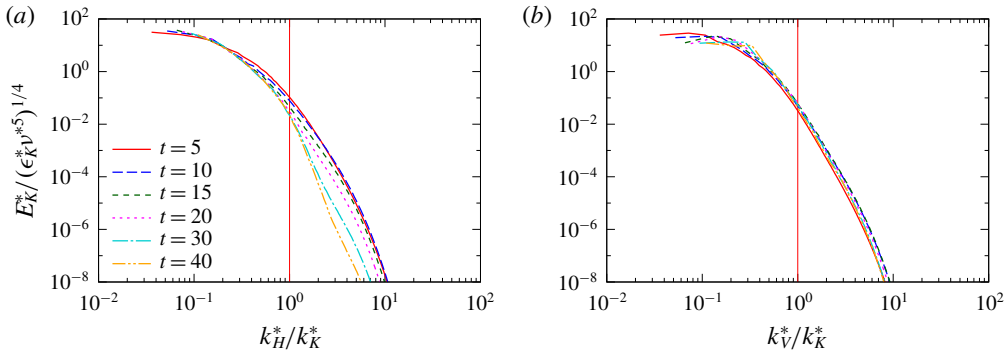
FIGURE 16. (Colour online) Normalised kinetic-energy spectrum for $Pr = 70$: (a) horizontal spectrum and (b) vertical spectrum. The vertical solid line shows $k_H^*/k_K^* = 1$ or $k_V^*/k_K^* = 1$.

by the experiment using a salt-stratified fluid by Praud *et al.* (2005). However, the k_V^{-3} power law in the vertical spectrum they observed is not found in figure 16(b) because the Reynolds number is too small to realise such a constant slope in the low-wavenumber range in our simulations. The normalised spectrum of the vertical velocity in salt-stratified water experiments ($Pr = 700$) is presented in figure 19 of Itsweire *et al.* (1986), showing a slight dispersion at $k_x^*/k_K^* \gtrsim 10^0$. Though they attributed the dispersion of the spectra at high wavenumbers to experimental noise, the energy spectrum could actually deviate from the universal curve since the Kolmogorov scale approaches the Ozmidov scale far downstream of the water channel in their experiment (cf. their figures 4 and 8).

3.4. *Generation of the vertically thin structures in the density perturbation*

In the remainder of this paper, we discuss how the anisotropic distribution of the potential energy at high wavenumbers for high Prandtl numbers is generated. According to Batchelor (1959), the scalar fluctuations smaller than the Kolmogorov scale are generated by a straining motion of the fluid at the Kolmogorov scale. Thus, we examine the direction of the principal axes of the strain-rate tensor, which is defined by $S_{ij} = (\partial u_i/\partial x_j + \partial u_j/\partial x_i)/2$. Since the strain-rate tensor is a real-valued symmetric tensor, it has three principal values ($\alpha \geqslant \beta \geqslant \gamma$) and the corresponding principal axes ($\boldsymbol{\alpha}$, $\boldsymbol{\beta}$ and $\boldsymbol{\gamma}$) are orthogonal. The incompressibility condition ($\alpha + \beta + \gamma = 0$) requires $\alpha > 0$ and $\gamma < 0$. We consider the cosines of the angles between the principal axes and the vertical axis,

$$\cos\theta_{z\alpha} = \boldsymbol{e}_z \cdot \boldsymbol{\alpha}, \quad \cos\theta_{z\beta} = \boldsymbol{e}_z \cdot \boldsymbol{\beta}, \quad \cos\theta_{z\gamma} = \boldsymbol{e}_z \cdot \boldsymbol{\gamma}, \quad (3.14a\text{--}c)$$

and the cosine of the angle between the density gradient and the vertical axis,

$$\cos\theta_{z\rho'} = \boldsymbol{e}_z \cdot \frac{\boldsymbol{\nabla}\rho'}{|\boldsymbol{\nabla}\rho'|}, \quad (3.15)$$

where $\boldsymbol{e}_z$ is the unit vector in the vertical direction.

Figure 17(a) presents the probability density functions (p.d.f.s) of $|\cos\theta_{z\alpha}|$, $|\cos\theta_{z\beta}|$, $|\cos\theta_{z\gamma}|$ and $|\cos\theta_{z\rho'}|$ for $Pr = 70$ at $t = 4$. The highest probability of
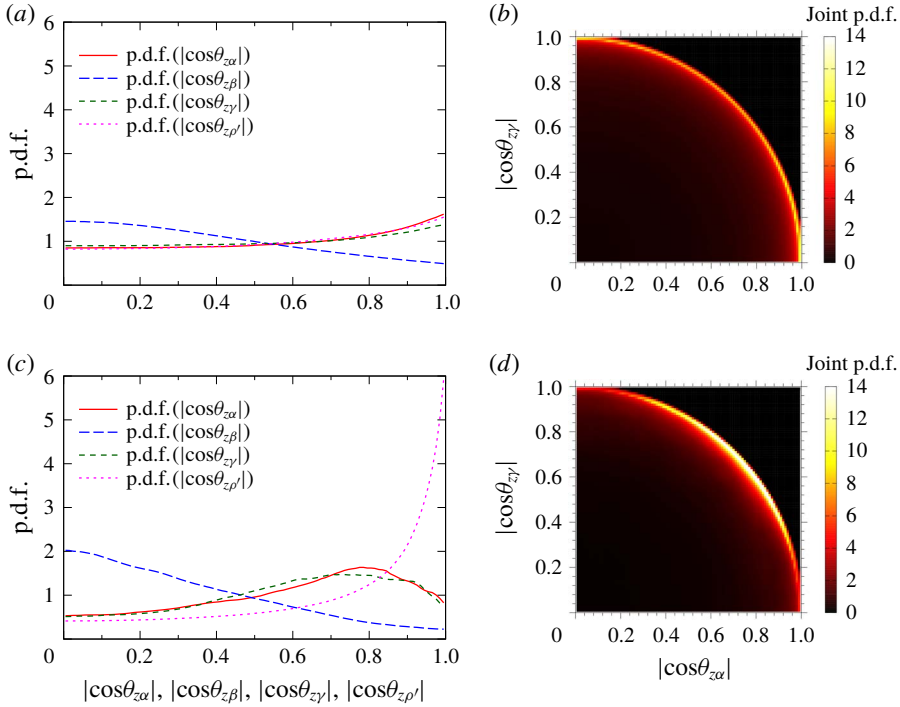
FIGURE 17. (Colour online) (*a,c*) The p.d.f.s of $|\cos\theta_{z\alpha}|$, $|\cos\theta_{z\beta}|$, $|\cos\theta_{z\gamma}|$ and $|\cos\theta_{z\rho'}|$ for $Pr = 70$. (*b,d*) Joint p.d.f.s of $|\cos\theta_{z\alpha}|$ and $|\cos\theta_{z\gamma}|$ for $Pr = 70$. Time (*a,b*) $t = 4$ and (*c,d*) $t = 40$.

$|\cos\theta_{z\alpha}|$ and $|\cos\theta_{z\gamma}|$ occurs when $|\cos\theta_{z\alpha}| = 1$ (or $\theta_{z\alpha} = 0$, π) and $|\cos\theta_{z\gamma}| = 1$ (or $\theta_{z\gamma} = 0$, π), respectively, indicating that the most expansive direction ($\boldsymbol{\alpha}$) and the most contractive direction ($\boldsymbol{\gamma}$) tend to align with the vertical axis probably because of the Brunt–Väisälä oscillation due to the buoyancy. However, $\boldsymbol{\alpha}$ and $\boldsymbol{\gamma}$ cannot align with the vertical axis at the same time because they are orthogonal. This can be confirmed by the joint p.d.f. of $|\cos\theta_{z\alpha}|$ and $|\cos\theta_{z\gamma}|$ in figure 17(*b*). There are two local maxima at $(|\cos\theta_{z\alpha}|, |\cos\theta_{z\gamma}|) = (0, 1)$ and $(1, 0)$. Also, the probability density of $|\cos\theta_{z\beta}|$ becomes largest when $|\cos\theta_{z\beta}| = 0$ (or $\theta_{z\beta} = \pi/2$), as shown in figure 17(*a*). After all, at an early time of $t = 4$, either the most expansive direction ($\boldsymbol{\alpha}$) or the most contractive direction ($\boldsymbol{\gamma}$) tends to be along the vertical axis, while the other two principal axes are horizontal. The p.d.f.s of $|\cos\theta_{z\alpha}|$, $|\cos\theta_{z\beta}|$ and $|\cos\theta_{z\gamma}|$ are nearly independent of time until the Ozmidov wavenumber approaches the Kolmogorov wavenumber ($3 \lesssim t \lesssim 6$). Figure 17(*a*) also shows that the probability density of $|\cos\theta_{z\rho'}|$ becomes highest at $|\cos\theta_{z\rho'}| = 1$, indicating that the density gradient $\nabla\rho'$ tends to be vertical and the horizontally flat distribution of density begins to be generated.

Figure 17(*c*) shows the p.d.f.s at $t = 40$. The p.d.f.s of $|\cos\theta_{z\alpha}|$ and $|\cos\theta_{z\gamma}|$ have a peak at $|\cos\theta_{z\alpha}| \sim 0.8$ and $|\cos\theta_{z\gamma}| \sim 0.7$, respectively. The joint p.d.f. of $|\cos\theta_{z\alpha}|$ and $|\cos\theta_{z\gamma}|$ in figure 17(*d*) displays only one peak at $|\cos\theta_{z\alpha}| \sim |\cos\theta_{z\gamma}| \sim 0.7 \sim 1/\sqrt{2}$, meaning that both the most expansive direction ($\boldsymbol{\alpha}$) and the most contractive direction ($\boldsymbol{\gamma}$) tend to make an angle of 45° with the vertical axis. This situation occurs when the vertical shear of the horizontal flow is dominant in the strain-rate tensor (appendix A).

The transition to the p.d.f.s corresponding to the vertically sheared horizontal flow takes place when the Ozmidov wavenumber becomes as large as the Kolmogorov wavenumber ($t \sim 8$ for $Pr = 70$). Smyth (1999) also reported that $\boldsymbol{\alpha}$ and $\boldsymbol{\gamma}$ point at 45° from the vertical after the stratified shear turbulence triggered by the Kelvin–Helmholtz instability had decayed ($Re_b \to 1$) and the flow exhibits a pancake structure. The p.d.f. of $|\cos\theta_{z\rho'}|$ shows that the density gradient tends to direct towards the vertical axis, and the tendency is much more significant compared to the case of $t = 4$.

In order to investigate whether the vertically sheared horizontal flow is dominant at late times in our simulation, we decompose the kinetic-energy dissipation rate into four components:

$$\epsilon_{H,H} = \frac{1}{Re_0} \overline{\left(\frac{\partial u}{\partial x}\right)^2 + \left(\frac{\partial u}{\partial y}\right)^2 + \left(\frac{\partial v}{\partial x}\right)^2 + \left(\frac{\partial v}{\partial y}\right)^2} \quad (\text{horizontal shear of horizontal flow}),$$

(3.16)

$$\epsilon_{H,V} = \frac{1}{Re_0} \overline{\left(\frac{\partial u}{\partial z}\right)^2 + \left(\frac{\partial v}{\partial z}\right)^2} \quad (\text{vertical shear of horizontal flow}), \quad (3.17)$$

$$\epsilon_{V,H} = \frac{1}{Re_0} \overline{\left(\frac{\partial w}{\partial x}\right)^2 + \left(\frac{\partial w}{\partial y}\right)^2} \quad (\text{horizontal shear of vertical flow}), \quad (3.18)$$

and

$$\epsilon_{V,V} = \frac{1}{Re_0} \overline{\left(\frac{\partial w}{\partial z}\right)^2} \quad (\text{vertical shear of vertical flow}), \quad (3.19)$$

where

$$\epsilon_K = \epsilon_{H,H} + \epsilon_{H,V} + \epsilon_{V,H} + \epsilon_{V,V}. \quad (3.20)$$

The contribution from the vertical shear of the horizontal flow, $\epsilon_{H,V}$, is expected to be dominant at late times of our simulation. Note that it is not equal to the kinetic-energy dissipation rate of the VSHF (vertically sheared horizontal flow) mode (Smith & Waleffe 2002) because $\epsilon_{H,V}$ includes Fourier modes of $k_H = \sqrt{k_x^2 + k_y^2} \neq 0$. For an isotropic turbulence (Taylor 1935),

$$\overline{\left(\frac{\partial u}{\partial x}\right)^2} = \overline{\left(\frac{\partial v}{\partial y}\right)^2} = \overline{\left(\frac{\partial w}{\partial z}\right)^2} = \frac{1}{15}\overline{\left(\frac{\partial u_i}{\partial x_j}\right)^2}, \quad (3.21)$$

and

$$\overline{\left(\frac{\partial u}{\partial y}\right)^2} = \overline{\left(\frac{\partial u}{\partial z}\right)^2} = \overline{\left(\frac{\partial v}{\partial x}\right)^2} = \overline{\left(\frac{\partial v}{\partial z}\right)^2} = \overline{\left(\frac{\partial w}{\partial x}\right)^2} = \overline{\left(\frac{\partial w}{\partial y}\right)^2} = \frac{2}{15}\overline{\left(\frac{\partial u_i}{\partial x_j}\right)^2}, \quad (3.22)$$

lead to

$$\frac{\epsilon_{H,H}}{\epsilon_K} = \frac{6}{15}, \quad \frac{\epsilon_{H,V}}{\epsilon_K} = \frac{4}{15}, \quad \frac{\epsilon_{V,H}}{\epsilon_K} = \frac{4}{15}, \quad \frac{\epsilon_{V,V}}{\epsilon_K} = \frac{1}{15}. \quad (3.23a-d)$$

Temporal variation of these ratios in stratified flow at $Pr = 70$ is presented in figure 18(a), illustrating the deviation from their isotropic values. After $t \sim 8$, $\epsilon_{H,V}/\epsilon_K$ rapidly increases, and it eventually reaches ~ 0.6, while $\epsilon_{H,H}/\epsilon_K$ and $\epsilon_{V,H}/\epsilon_K$ become
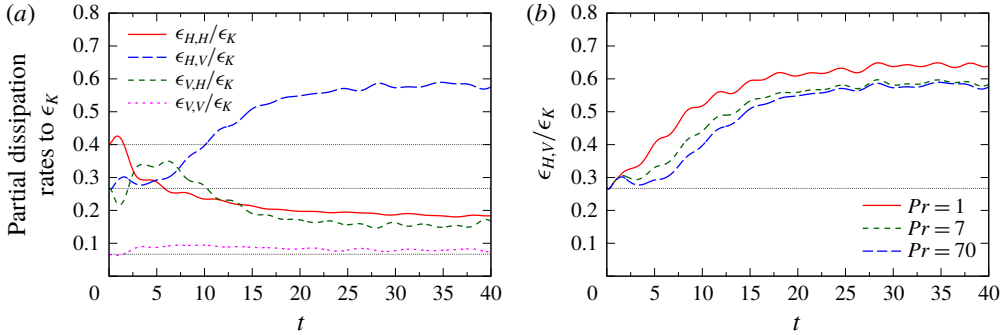
FIGURE 18. (Colour online) (*a*) Temporal variations of the ratios of $\epsilon_{H,H}$, $\epsilon_{H,V}$, $\epsilon_{V,H}$ and $\epsilon_{V,V}$ to the kinetic-energy dissipation rate ϵ_K for $Pr = 70$. The horizontal dotted lines indicate the values for isotropic turbulence: 1/15, 4/15 and 6/15 from below. (*b*) The *Pr* dependence of $\epsilon_{H,V}/\epsilon_K$.

significantly smaller than their isotropic values. The salt-stratified experiments by Fincham *et al.* (1996) and Praud *et al.* (2005) reported a higher value of $\epsilon_{H,V}/\epsilon_K \sim 0.9$. The smaller $\epsilon_{H,V}/\epsilon_K$ in our simulation would not be due to the low-Prandtl-number effect because $\epsilon_{H,V}/\epsilon_K$ generally decreases with increasing Prandtl number (figure 18*b*). As the previous numerical simulations by Hebert & de Bruyn Kops (2006) report the Reynolds-number dependence of $\epsilon_{H,V}/\epsilon_K$, in which $\epsilon_{H,V}/\epsilon_K$ decreases with decreasing Reynolds number at low Reynolds numbers (see their figure 1), the difference in $\epsilon_{H,V}/\epsilon_K$ might be caused by the small Reynolds number of our simulation.

We next apply an analysis similar to Batchelor (1959) to the late stage of decaying stratified turbulence, i.e. after a certain large time t_0 (typically $t_0 > 20$; cf. figure 18) for which the vertically sheared horizontal flow is dominant down to the Kolmogorov scale. A brief review of the theory for a high-*Pr* passive scalar by Batchelor (1959) is given in appendix B. We consider the deformation of a fluid element whose linear dimension is slightly smaller than the Kolmogorov scale, and whose translational velocity is $\boldsymbol{u}_{el}(t) = (u_{el}, v_{el}, w_{el})$. New spatial coordinates $\boldsymbol{X} = (X, Y, Z)$ which translate with the fluid element are introduced, but, unlike in Batchelor (1959), they do not rotate, so that the X, Y and Z axes are always parallel to the x, y and z axes, respectively. Then, the new coordinate axes do not necessarily agree with the principal axes of the strain-rate tensor. Assuming that $\boldsymbol{X} = \boldsymbol{x}$ at $t = t_0$, i.e. the fluid element is initially located at $\boldsymbol{x} = \boldsymbol{0}$, the spatial coordinates $\boldsymbol{X}$ are defined by

$$\boldsymbol{X} = \boldsymbol{x} - \int_{t_0}^{t} \boldsymbol{u}_{el}(\tau) \, \mathrm{d}\tau. \tag{3.24}$$

A new temporal coordinate T, which represents the elapsed time after $t = t_0$, is also introduced, defined by

$$T = t - t_0. \tag{3.25}$$

If we assume that the velocity in the translational coordinates, (U, V, W), is dominated by vertically sheared horizontal flow, i.e. $(U, V, W) = (S_X Z, S_Y Z, 0)$, the transport equation of the density perturbation (2.2) becomes

$$\frac{\partial \rho'}{\partial T} + S_X Z \frac{\partial \rho'}{\partial X} + S_Y Z \frac{\partial \rho'}{\partial Y} = \frac{1}{Re_0 Pr} \left(\frac{\partial^2 \rho'}{\partial X^2} + \frac{\partial^2 \rho'}{\partial Y^2} + \frac{\partial^2 \rho'}{\partial Z^2} \right) + w_{el}(t_0 + T), \tag{3.26}$$
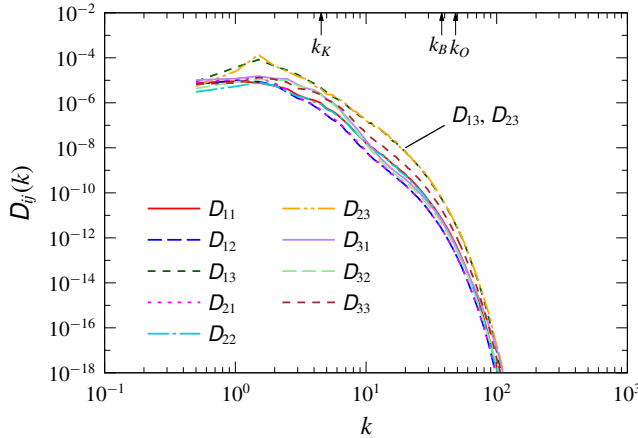
FIGURE 19. (Colour online) Kinetic-energy dissipation spectrum tensor, D_{ij}, at $t = 40$ for $Pr = 70$. The Kolmogorov, Ozmidov and Batchelor wavenumbers for $Pr = 70$ are indicated by the arrows at the top of the panel.

in the frame of reference moving with the fluid element. The detailed derivation of (3.26) is presented in appendix C.

The assumption that the flow at scales smaller than the Kolmogorov scale is dominated by the vertical shear of the horizontal flow at late times is verified again by examining the kinetic-energy dissipation spectrum tensor, which is defined by

$$D_{ij}(k) = \sum_{\left| \sqrt{k_x^2 + k_y^2 + k_z^2} - k \right| < k_{min}/2} \frac{k_j^2}{Re_0} |\hat{u}_i(k_x, k_y, k_z)|^2 \frac{1}{k_{min}}, \quad (3.27)$$

(no summation is taken over the repeated indices i and j), and satisfies

$$\frac{1}{Re_0} \overline{\left(\frac{\partial u_i}{\partial x_j} \right)^2} = \int_0^\infty D_{ij}(k)\, \mathrm{d}k. \quad (3.28)$$

As shown in figure 19, the contributions from the vertical shear of the horizontal flow (D_{13} and D_{23}) are greater than the other components at all wavenumbers at $t = 40$ for $Pr = 70$, but they are close to D_{31}, D_{32} and D_{33} at $k \sim k_K$, indicating that the assumption of the vertically sheared horizontal flow holds moderately well.

The magnitude of the strain rate S_X ($\simeq S_Y$) is estimated from figure 18 as follows:

$$\frac{\epsilon_{H,V}}{\epsilon_K} = \frac{\overline{(\partial u/\partial z)^2} + \overline{(\partial v/\partial z)^2}}{Re_0 \epsilon_K} \simeq \frac{2S_X^2}{Re_0 \epsilon_K} \simeq 0.5 \quad \text{at } t \gtrsim 20, \quad (3.29)$$

which gives

$$|S_X| \simeq \frac{1}{2} \sqrt{Re_0 \epsilon_K} \quad \text{or} \quad |S_X^*| \simeq \frac{1}{2} \sqrt{\frac{\epsilon_K^*}{\nu^*}} = \frac{1}{2t_K^*}, \quad (3.30a,b)$$

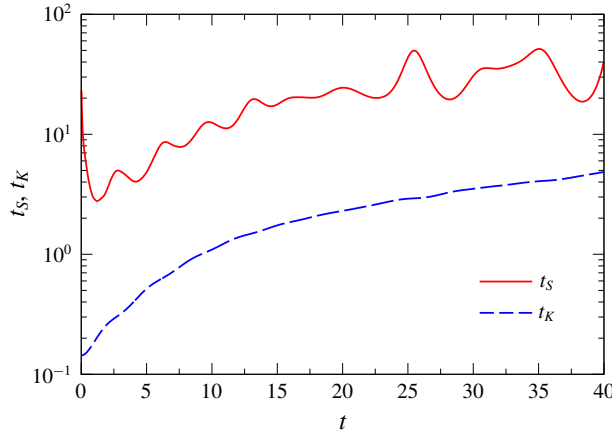where t_K^* is the dimensional Kolmogorov time.

FIGURE 20. (Colour online) The evolution of the time scale of change of the mean shear rate t_S and the Kolmogorov time t_K at $Pr = 70$.

If we define the mean shear rate S by

$$S = \left(\frac{\overline{(\partial u/\partial z)^2} + \overline{(\partial v/\partial z)^2}}{2} \right)^{1/2}, \tag{3.31}$$

it would vary in the time scale of

$$t_S = -\frac{S}{\mathrm{d}S/\mathrm{d}t}. \tag{3.32}$$

The time scale t_S for the case of $Pr = 70$ is plotted with the Kolmogorov time in figure 20, showing that t_S is one order of magnitude larger than t_K. Thus, in the following analysis, we assume that the shear rate (S_X, S_Y) is steady during the Kolmogorov time. We mention here, however, that a Lagrangian analysis (e.g. Girimaji & Pope 1990) is necessary to validate the assumption of steady shearing, since we consider here that the coordinates translate with the fluid element. For isotropic turbulence, Kraichnan's spectrum, which takes into account the unsteadiness of the strain rates, often fits the previous DNS results (Bogucki *et al.* 1997; Smyth 1999) better than Batchelor's spectrum, which assumes steady straining.

We now seek a solution of (3.26) in the form of

$$\rho'(\boldsymbol{X}, T) = A(T) \sin(\boldsymbol{m}(T) \cdot \boldsymbol{X}) + \int_0^T w_{el}(t_0 + \tau) \, \mathrm{d}\tau, \tag{3.33}$$

with an initial condition of $A(0) = A_0$ and $\boldsymbol{m}(0) = (m_{X0}, m_{Y0}, m_{Z0})$. Substitution of (3.33) into (3.26) gives four ordinary differential equations:

$$\frac{\mathrm{d}m_X}{\mathrm{d}T} = 0, \quad \frac{\mathrm{d}m_Y}{\mathrm{d}T} = 0, \quad \frac{\mathrm{d}m_Z}{\mathrm{d}T} = -(S_X m_X + S_Y m_Y), \tag{3.34a-c}$$

and

$$\frac{\mathrm{d}A}{\mathrm{d}T} = -\frac{m_X^2 + m_Y^2 + m_Z^2}{Re_0 Pr} A, \tag{3.35}$$

which can be solved as

$$m_X = m_{X0}, \quad m_Y = m_{Y0}, \quad m_Z = m_{Z0} - (S_X m_{X0} + S_Y m_{Y0})T, \qquad (3.36a-c)$$

and

$$A(T) = A_0 \exp \left[-\frac{1}{Re_0 Pr} \left\{ (m_{X0}^2 + m_{Y0}^2 + m_{Z0}^2)T \right. \right.$$
$$\left. \left. - m_{Z0}(S_X m_{X0} + S_Y m_{Y0})T^2 + \frac{1}{3}(S_X m_{X0} + S_Y m_{Y0})^2 T^3 \right\} \right]. \qquad (3.37)$$

Invariance of the horizontal wavenumbers m_X and m_Y indicates that the vertically sheared horizontal flow does not alter the horizontal scale of density perturbation. The vertical wavenumber m_Z increases linearly with time, and the increase during the Kolmogorov time t_K can be estimated using (3.30) and (3.36) as

$$|\Delta m_Z| = |m_Z(t_K) - m_{Z0}| = |S_X m_{X0} + S_Y m_{Y0}| t_K \lesssim \frac{|m_{X0}| + |m_{Y0}|}{2} \simeq |m_{X0}|. \qquad (3.38)$$

This would not be large when the flow has a large horizontal scale. Then, the wavenumber vector $\boldsymbol{m}$ would become aligned with the vertical axis slowly if observed in the Kolmogorov time scale, and the density gradient finally directs upwards (cf. figure 17c). The increase of the vertical wavenumber of fluid elements would explain why the vertical spectrum of potential energy $E_P(k_V)$ below the Kolmogorov scale becomes larger than the horizontal spectrum $E_P(k_H)$ at late times, as observed in figure 15.

We note that the second term on the right-hand side of (3.33) shows the variation of density perturbation due to the vertical movement of the fluid element. The density perturbation increases (or decreases) when the vertical velocity of the fluid element is positive (or negative), since the background density field is stably stratified. However, this term is a function of only T (and t_0) and is independent of X, and adds the same density perturbation to every point in the fluid. Therefore, it has no dynamical effects.

In the present numerical simulation, the small-scale vertical structure of the potential energy has been observed only at the highest Prandtl number ($Pr = 70$), but has not been observed at lower Prandtl numbers ($Pr = 1$ and 7; cf. figures 10 and 11). The reason would be explained by (3.37), considering a fluid element with an initial disturbance of wavenumber $|\boldsymbol{m}(0)| = \alpha k_K$, where α is a constant of order unity. The amplitude decay during the Kolmogorov time can be estimated from (3.37) as

$$\frac{A(t_K)}{A_0} \simeq \exp \left(-\frac{\alpha^2 k_K^2 t_K}{Re_0 Pr} \right) = \exp \left(-\frac{\alpha^2}{Pr} \right). \qquad (3.39)$$

If the Prandtl number is not large ($Pr = O(\alpha^2) = O(1)$), the density perturbation decreases to $1/e$ of its initial value during the Kolmogorov time. This means that the density perturbations would decay before the vertically small-scale density distribution is generated in a time typically much longer than t_K. When the vertically small-scale components are generated in the density perturbation, corresponding small-scale components of velocity would be generated through the vertical density flux. However, the latter components would also decay in the Kolmogorov time, and will not affect the vertical scale of the velocity perturbation.

The present form of solution is very similar to the previous result by the RDT, which takes into account the initial condition (Hanazaki & Hunt 2004). The main differences are that the present result is intended for a small-scale phenomenon near the Kolmogorov scale, and the Prandtl number is not limited to $Pr = 1$. Both results show, however, that the temporal variation of wavenumber vector $\boldsymbol{m}(T)$ and the amplitude of perturbation $A(T)$ are determined only by the shear (cf. Townsend 1976), and irrelevant to the stratification even when the scalar is buoyant. The present results indeed reduce to equations (2.6) and (4.4) of Hanazaki & Hunt (2004), under the condition of $Pr = 1$ and $S_Y = 0$.

We finally mention that the nonlinear advection terms in the Navier–Stokes equations and the density equation vanish for the vertically sheared horizontal flow, and such a flow is governed exactly by the linear equations (Majda & Grote 1997). Therefore, the flow dominated by the vertically sheared horizontal flow would be described well by the linear theory.

4. Conclusions

We have investigated the decaying turbulence in a density-stratified fluid of a high Prandtl number up to $Pr = 70$ through a direct numerical simulation. The main results of this study are summarised as follows.

The kinetic and potential energies decay more slowly for higher Prandtl numbers, since the scalar fluctuations of a higher Prandtl number dissipate more slowly and more potential energy can be converted into vertical kinetic energy through the vertical density flux, which is more negative and more counter-gradient. The Prandtl-number effect is generally less significant for the velocity fluctuation (e.g. KE and ϵ_K) than the density fluctuation (e.g. PE and ϵ_P), since the effect of molecular diffusion becomes conspicuous at scales smaller than the Kolmogorov scale.

The difference due to the increase of the Prandtl number becomes less significant for larger Pr (e.g. for $Pr \gtrsim 7$), although there is no upper threshold value of Pr at which further Pr dependence completely disappears. Since the molecular-diffusion term in the governing equation is proportional to $1/Pr$, the direct effect of molecular diffusion is already small at $Pr = 7$ compared to that at $Pr = 1$, if the spatial structure of the density distribution is the same. Therefore, further increase of Pr from 7 to 70, or to 700, will not significantly reduce the value of $1/Pr$ (i.e. from $1/7$ to $1/70$, or to $1/700$), and the effects of those Pr increments would be small. The large-scale components are more insensitive to the increase of Pr since the scalar diffusion is not significant at large scales, while the small-scale components, especially those smaller than the Kolmogorov scale, are more susceptible to the increase of Pr which generates new small-scale structures.

The buoyancy effect is initially limited to large scales, but extends gradually to smaller scales, and the density fluctuations smaller than the Kolmogorov scale show very different structures before and after they are affected by the buoyancy. Before the buoyancy becomes effective down to the Kolmogorov scale ($k_O < k_K$ and $Re_b > 1$), the fluid motion is nearly isotropic at small scales, and the density behaves just like a passive scalar in isotropic turbulence. Indeed, the kinetic and potential energy have very similar horizontal and vertical spectra (i.e. $E_K(k_H) \sim E_K(k_V)$ and $E_P(k_H) \sim E_P(k_V)$ for the same k_H and k_V), and the potential energy shows a k^{-1} spectrum in the viscous–convective subrange ($k_K \lesssim k_H \lesssim k_B$ and $k_K \lesssim k_V \lesssim k_B$) at the highest Pr ($= 70$).

After the buoyancy becomes effective below the Kolmogorov scale ($k_K < k_O$ and $Re_b < 1$), the kinetic- and potential-energy distributions show pancake structures.

The horizontal scales of these pancakes are comparable for all $Pr(= 1, 7, 70)$, but the vertical scale of potential-energy distribution is smaller for higher Pr, and the pancakes at the highest Pr $(= 70)$ have horizontal wrinkles on their surface. Correspondingly, the vertical spectrum below the Kolmogorov scale is larger than the horizontal spectrum (i.e. $E_P(k_V) > E_P(k_H)$ for the same k_H and k_V $(>k_K)$), and the potential energy no longer follows the k^{-1} spectrum.

As long as the buoyancy Reynolds number Re_b is larger than unity, the normalised kinetic-energy spectrum follows the Kolmogorov scaling and the normalised potential-energy spectrum follows the Batchelor scaling. However, after Re_b falls below unity, the horizontal spectra no longer collapse onto a single curve below the Kolmogorov scale, while the curves of vertical spectra continue to collapse there.

The small-scale anisotropy of potential energy observed when $Re_b < 1$ is generated by the vertically sheared horizontal flow at the Kolmogorov scale. Its dominance could be shown by p.d.f.s for the angles between the vertical axis and the principal axes of the strain-rate tensor, and by the contribution to the total kinetic-energy dissipation. Our theoretical analysis similar to Batchelor (1959) shows that the vertically sheared horizontal flow at the Kolmogorov scale reduces the vertical scale of density fluctuations, but does not change the horizontal scale.

We finally discuss how the Prandtl-number effect investigated in this paper will change for a different initial Reynolds number Re_0 or a different initial Froude number Fr_0. If the Reynolds number increases, the difference between the energy-containing scale and the Kolmogorov scale becomes larger. Then, the large-scale quantities such as energy will become more insensitive to the Prandtl number, while the small-scale quantities such as the energy-dissipation rate are still normally affected by the Prandtl number. If the Froude number decreases, or if the Brunt–Väisälä frequency N^* increases, the buoyancy Reynolds number Re_b $(= \epsilon_K^*/(\nu^* N^{*2}))$ will decrease since the kinetic-energy dissipation rate ϵ_K^* will not change significantly (Bartello & Tobias 2013). The reduction of Re_b means that the effect of stratification becomes more significant and the nonlinear effect becomes weaker, so that the molecular effect of the Prandtl number becomes more conspicuous.

Acknowledgements

Appendix A. Principal axes of the vertically sheared horizontal flow

We derive here the angles between the vertical axis and the principal axes of the strain-rate tensor of the vertically sheared horizontal flow, in which only $\partial u/\partial z$ and $\partial v/\partial z$ are non-zero and the other elements are zero. The principal values of the strain-rate tensor are

$$\alpha = \frac{1}{2}\sqrt{\left(\frac{\partial u}{\partial z}\right)^2 + \left(\frac{\partial v}{\partial z}\right)^2}, \quad \beta = 0, \quad \gamma = -\frac{1}{2}\sqrt{\left(\frac{\partial u}{\partial z}\right)^2 + \left(\frac{\partial v}{\partial z}\right)^2}, \quad (A\,1a{-}c)$$

and the corresponding principal axes are

$$\boldsymbol{\alpha} = \begin{pmatrix} (\partial u/\partial z)/(2\|\boldsymbol{S}\|) \\ (\partial v/\partial z)/(2\|\boldsymbol{S}\|) \\ 1/\sqrt{2} \end{pmatrix}, \quad \boldsymbol{\beta} = \begin{pmatrix} (\partial v/\partial z)/\sqrt{(2\|\boldsymbol{S}\|)} \\ -(\partial u/\partial z)/\sqrt{(2\|\boldsymbol{S}\|)} \\ 0 \end{pmatrix}, \quad \boldsymbol{\gamma} = \begin{pmatrix} -(\partial u/\partial z)/(2\|\boldsymbol{S}\|) \\ -(\partial v/\partial z)/(2\|\boldsymbol{S}\|) \\ 1/\sqrt{2} \end{pmatrix},$$

$$(A\,2a{-}c)$$

where $\|\boldsymbol{S}\| = \sqrt{\{(\partial u/\partial z)^2 + (\partial v/\partial z)^2\}/2}$ is the Frobenius norm of the strain-rate tensor. Then, both $\theta_{z\alpha}$ and $\theta_{z\gamma}$ become $\pi/4$, and $\theta_{z\beta}$ becomes $\pi/2$ since $\boldsymbol{e}_z \cdot \boldsymbol{\alpha} = \boldsymbol{e}_z \cdot \boldsymbol{\gamma} = 1/\sqrt{2}$ and $\boldsymbol{e}_z \cdot \boldsymbol{\beta} = 0$.

Appendix B. Review of the theory for a high-*Pr* passive scalar (Batchelor 1959)

Here is a brief review of the theory by Batchelor (1959), which describes the sub-Kolmogorov behaviour of a high-*Pr* passive scalar in isotropic turbulence. He considered a material element of fluid whose dimension is smaller than the Kolmogorov scale, and with an initially sinusoidal variation of the high-*Pr* scalar. The length scale of change of the velocity gradient is assumed to be larger than the Kolmogorov scale, and the principal values of the strain-rate tensor are constant for time intervals at least as large as the Kolmogorov time. Then, the element is in effect distorted by a purely straining motion of a constant magnitude. Choosing the Cartesian coordinates, (X, Y, Z), which translate and rotate with the element and which correspond to the principal axes of the strain-rate tensor of the element, the convection–diffusion equation of the scalar θ in the non-dimensional form becomes

$$\frac{\partial \theta}{\partial t} + \alpha X \frac{\partial \theta}{\partial X} + \beta Y \frac{\partial \theta}{\partial Y} + \gamma Z \frac{\partial \theta}{\partial Z} = \frac{1}{Re_0 Pr} \left(\frac{\partial^2 \theta}{\partial X^2} + \frac{\partial^2 \theta}{\partial Y^2} + \frac{\partial^2 \theta}{\partial Z^2} \right), \quad \text{(B 1)}$$

where the largest principal value of the strain-rate tensor, α, and the smallest principal value, γ, satisfy $\alpha > 0$ and $\gamma < 0$, respectively, because of the incompressibility condition ($\alpha + \beta + \gamma = 0$). Equation (B 1) is satisfied by $\theta(\boldsymbol{X}, t) = A(t) \sin(\boldsymbol{m}(t) \cdot \boldsymbol{X})$, with

$$\frac{\mathrm{d}m_X}{\mathrm{d}t} = -\alpha m_X, \quad \frac{\mathrm{d}m_Y}{\mathrm{d}t} = -\beta m_Y, \quad \frac{\mathrm{d}m_Z}{\mathrm{d}t} = -\gamma m_Z, \quad \text{and} \quad \frac{\mathrm{d}A}{\mathrm{d}t} = -\frac{m_X^2 + m_Y^2 + m_Z^2}{Re_0 Pr} A, \quad \text{(B 2a–d)}$$

where the wavenumber vector $\boldsymbol{m} = (m_X, m_Y, m_Z)$. The solution with the initial condition $A(0) = A_0$ and $\boldsymbol{m}(0) = (m_{X0}, m_{Y0}, m_{Z0})$ is

$$\boldsymbol{m}(t) = (m_{X0} \exp(-\alpha t), m_{Y0} \exp(-\beta t), m_{Z0} \exp(-\gamma t)), \quad \text{(B 3)}$$

and

$$A(t) = A_0 \exp \left[\frac{1}{2Re_0 Pr} \left(\frac{m_X^2 - m_{X0}^2}{\alpha} + \frac{m_Y^2 - m_{Y0}^2}{\beta} + \frac{m_Z^2 - m_{Z0}^2}{\gamma} \right) \right]. \quad \text{(B 4)}$$

For a sufficiently large t, the solution asymptotes to

$$|\boldsymbol{m}|^2 \to m_{Z0}^2 \exp(-2\gamma t) \quad \text{and} \quad A \to A_0 \exp \left(\frac{|\boldsymbol{m}|^2}{2\gamma Re_0 Pr} \right). \quad \text{(B 5a,b)}$$

This shows that the small-scale fluctuations are generated in the most contractive direction (Z direction), and the planes of constant θ are turned so that the direction of their normal, $\boldsymbol{m}$, approaches asymptotically the direction of the greatest rate of contraction.

Appendix C. Transport equation of the density perturbation in the reference frame moving with the fluid element

We consider the transformation of the transport equation of the density perturbation in the stationary coordinates $(\boldsymbol{x}, t)$ into that in the translational coordinates $(\boldsymbol{X}, T)$. These two coordinates are related by

$$\boldsymbol{X} = \boldsymbol{x} - \int_{t_0}^{t} \boldsymbol{u}_{el}(\tau)\,\mathrm{d}\tau, \quad \text{and} \quad T = t - t_0, \tag{C 1a,b}$$

where $\boldsymbol{u}_{el}(t) = (u_{el}, v_{el}, w_{el})$ is the velocity of the fluid element relative to the stationary coordinates and t_0 is a time at which $Re_b \ll 1$ is satisfied. Let the density perturbation in the translational coordinates be $\varrho'(\boldsymbol{X}, T)$ $(= \rho'(\boldsymbol{x}, t))$. Then, the partial derivatives with respect to the variables in the stationary coordinates are rewritten by using the chain rule as

$$\frac{\partial \rho'}{\partial t} = \frac{\partial \varrho'}{\partial T}\frac{\partial T}{\partial t} + \frac{\partial \varrho'}{\partial X}\frac{\partial X}{\partial t} + \frac{\partial \varrho'}{\partial Y}\frac{\partial Y}{\partial t} + \frac{\partial \varrho'}{\partial Z}\frac{\partial Z}{\partial t} = \frac{\partial \varrho'}{\partial T} - u_{el}\frac{\partial \varrho'}{\partial X} - v_{el}\frac{\partial \varrho'}{\partial Y} - w_{el}\frac{\partial \varrho'}{\partial Z}, \tag{C 2}$$

$$\frac{\partial \rho'}{\partial x} = \frac{\partial \varrho'}{\partial X}, \quad \frac{\partial \rho'}{\partial y} = \frac{\partial \varrho'}{\partial Y}, \quad \text{and} \quad \frac{\partial \rho'}{\partial z} = \frac{\partial \varrho'}{\partial Z}. \tag{C 3a–c}$$

Substituting the above relations into (2.2) leads to the transport equation of the density perturbation in the frame of reference moving with the fluid element,

$$\frac{\partial \varrho'}{\partial T} + U\frac{\partial \varrho'}{\partial X} + V\frac{\partial \varrho'}{\partial Y} + W\frac{\partial \varrho'}{\partial Z} = \frac{1}{Re_0 Pr}\left(\frac{\partial^2 \varrho'}{\partial X^2} + \frac{\partial^2 \varrho'}{\partial Y^2} + \frac{\partial^2 \varrho'}{\partial Z^2}\right) + W + w_{el}(t_0 + T), \tag{C 4}$$

where $\boldsymbol{U} = (U, V, W)$ is the velocity in the translational coordinates and satisfies

$$\boldsymbol{U} = \frac{\mathrm{d}\boldsymbol{X}}{\mathrm{d}t} = \boldsymbol{u} - \boldsymbol{u}_{el}. \tag{C 5}$$

Assuming the vertically sheared horizontal flow $(U, V, W) = (S_X Z, S_Y Z, 0)$, we finally obtain

$$\frac{\partial \varrho'}{\partial T} + S_X Z\frac{\partial \varrho'}{\partial X} + S_Y Z\frac{\partial \varrho'}{\partial Y} = \frac{1}{Re_0 Pr}\left(\frac{\partial^2 \varrho'}{\partial X^2} + \frac{\partial^2 \varrho'}{\partial Y^2} + \frac{\partial^2 \varrho'}{\partial Z^2}\right) + w_{el}(t_0 + T), \tag{C 6}$$

which reduces to (3.26) by replacing ϱ' with ρ'.

REFERENCES

BARRY, M. E., IVEY, G. N., WINTERS, K. B. & IMBERGER, J. 2001 Measurements of diapycnal diffusivities in stratified fluids. *J. Fluid Mech.* **442**, 267–291.

BARTELLO, P. & TOBIAS, S. M. 2013 Sensitivity of stratified turbulence to the buoyancy Reynolds number. *J. Fluid Mech.* **725**, 1–22.

BATCHELOR, G. K. 1959 Small-scale variation of convected quantities like temperature in turbulent fluid. *J. Fluid Mech.* **5**, 113–133.

BOGUCKI, D., DOMARADZKI, J. A. & YEUNG, P. K. 1997 Direct numerical simulations of passive scalars with $Pr > 1$ advected by turbulent flow. *J. Fluid Mech.* **343**, 111–130.

BRETHOUWER, G., BILLANT, P., LINDBORG, E. & CHOMAZ, J. M. 2007 Scaling analysis and simulation of strongly stratified turbulent flows. *J. Fluid Mech.* **585**, 343–368.

DE BRUYN KOPS, S. M. 2015 Classical scaling and intermittency in strongly stratified Boussinesq turbulence. *J. Fluid Mech.* **775**, 436–463.

DOUGHERTY, J. P. 1961 The anisotropy of turbulence at the meteor level. *J. Atmos. Terr. Phys.* **21**, 210–213.

FINCHAM, A. M., MAXWORTHY, T. & SPEDDING, G. R. 1996 Energy dissipation and vortex structure in freely decaying, stratified grid turbulence. *Dyn. Atmos. Oceans* **23**, 155–169.

GARGETT, A. E. & HOLLOWAY, G. 1992 Sensitivity of the GFDL ocean model to different diffusivities for heat and salt. *J. Phys. Oceanogr.* **22**, 1158–1177.

GARGETT, A. E., MERRYFIELD, W. J. & HOLLOWAY, G. 2003 Direct numerical simulation of differential scalar diffusion in three-dimensional stratified turbulence. *J. Phys. Oceanogr.* **33**, 1758–1782.

GERZ, T. & YAMAZAKI, H. 1993 Direct numerical simulation of buoyancy-driven turbulence in stably stratified fluid. *J. Fluid Mech.* **249**, 415–440.

GIBSON, C. H. & SCHWARZ, W. H. 1963 The universal equilibrium spectra of turbulent velocity and scalar fields. *J. Fluid Mech.* **16**, 365–384.

GIRIMAJI, S. S. & POPE, S. B. 1990 Material-element deformation in isotropic turbulence. *J. Fluid Mech.* **220**, 427–458.

GODEFERD, F. S. & STAQUET, C. 2003 Statistical modelling and direct numerical simulations of decaying stably stratified turbulence. Part 2. Large-scale and small-scale anisotropy. *J. Fluid Mech.* **486**, 115–159.

GRANT, H. L., HUGHES, B. A., VOGEL, W. M. & MOILLIET, A. 1968 The spectrum of temperature fluctuations in turbulent flow. *J. Fluid Mech.* **34**, 423–442.

HANAZAKI, H. & HUNT, J. C. R. 1996 Linear processes in unsteady stably stratified turbulence. *J. Fluid Mech.* **318**, 303–337.

HANAZAKI, H. & HUNT, J. C. R. 2004 Structure of unsteady stably stratified turbulence with mean shear. *J. Fluid Mech.* **507**, 1–42.

HEBERT, D. A. & DE BRUYN KOPS, S. M. 2006 Relationship between vertical shear rate and kinetic energy dissipation rate in stably stratified flows. *Geophys. Res. Lett.* **33**, L06602.

ITSWEIRE, E. C., HELLAND, K. N. & VAN ATTA, C. W. 1986 The evolution of grid-generated turbulence in a stably stratified fluid. *J. Fluid Mech.* **162**, 299–338.

KIMURA, Y. & HERRING, J. R. 1996 Diffusion in stably stratified turbulence. *J. Fluid Mech.* **328**, 253–269.

KOMORI, S. & NAGATA, K. 1996 Effects of molecular diffusivities on counter-gradient scalar and momentum transfer in strongly stable stratification. *J. Fluid Mech.* **326**, 205–237.

KRAICHNAN, R. H. 1968 Small-scale structure of a scalar field convected by turbulence. *Phys. Fluids* **11**, 945–953.

LIENHARD, J. H. & VAN ATTA, C. W. 1990 The decay of turbulence in thermally stratified flow. *J. Fluid Mech.* **190**, 57–112.

LIN, J. T. & PAO, Y. H. 1979 Wakes in stratified fluids. *Annu. Rev. Fluid Mech.* **11**, 317–338.

LINDBORG, E. 2006 The energy cascade in a strongly stratified fluid. *J. Fluid Mech.* **550**, 207–242.

MAFFIOLI, A. 2017 Vertical spectra of stratified turbulence at large horizontal scales. *Phys. Rev. Fluids* **2**, 104802.

MAFFIOLI, A., BRETHOUWER, G. & LINDBORG, E. 2016 Mixing efficiency in stratified turbulence. *J. Fluid Mech.* **794**, R3.

MAFFIOLI, A. & DAVIDSON, P. A. 2016 Dynamics of stratified turbulence decaying from a high buoyancy Reynolds number. *J. Fluid Mech.* **786**, 210–233.

MAJDA, A. J. & GROTE, M. J. 1997 Model dynamics and vertical collapse in decaying strongly stratified flows. *Phys. Fluids* **9**, 2932–2940.

MÉTAIS, O. & HERRING, J. R. 1989 Numerical simulations of freely evolving turbulence in stably stratified fluids. *J. Fluid Mech.* **202**, 117–148.

ORSZAG, S. A. & PATTERSON, G. S. 1972 Numerical simulation of three-dimensional homogeneous isotropic turbulence. *Phys. Rev. Lett.* **28**, 76–79.

OZMIDOV, R. V. 1965 On the turbulent exchange in a stably stratified ocean. *Izv. Atmos. Ocean Phys.* **1**, 493–497.

PAO, Y. H. 1973 Measurements of internal waves and turbulence in two-dimensional stratified shear flows. *Boundary-Layer Meteorol.* **5**, 177–193.

PRAUD, O., FINCHAM, A. M. & SOMMERIA, J. 2005 Decaying grid turbulence in a strongly stratified fluid. *J. Fluid Mech.* **522**, 1–33.

RILEY, J. J. & DE BRUYN KOPS, S. M. 2003 Dynamics of turbulence strongly influenced by buoyancy. *Phys. Fluids* **15**, 2047–2059.

RILEY, J. J., METCALFE, R. W. & WEISSMAN, M. A. 1981 Direct numerical simulations of homogeneous turbulence in density-stratified fluids. In *Proceedings of AIP Conference on Nonlinear Properties of Internal Waves* (ed. B. J. West), pp. 79–112. American Institute of Physics.

ROGALLO, R. S. 1977 An ILLIAC program for the numerical simulation of homogeneous incompressible turbulence, NASA TM-73203.

SALEHIPOUR, H. & PELTIER, W. R. 2015 Diapycnal diffusivity, turbulent Prandtl number and mixing efficiency in Boussinesq stratified turbulence. *J. Fluid Mech.* **775**, 464–500.

SALEHIPOUR, H., PELTIER, W. R. & MASHAYEK, A. 2015 Turbulent diapycnal mixing in stratified shear flows: the influence of Prandtl number on mixing efficiency and transition at high Reynolds number. *J. Fluid Mech.* **773**, 178–223.

SMITH, L. M. & WALEFFE, F. 2002 Generation of slow large scales in forced rotating stratified turbulence. *J. Fluid Mech.* **451**, 145–168.

SMYTH, W. D. 1999 Dissipation-range geometry and scalar spectra in sheared stratified turbulence. *J. Fluid Mech.* **401**, 209–242.

STAQUET, C. & GODEFERD, F. S. 1998 Statistical modelling and direct numerical simulations of decaying stably stratified turbulence. Part 1. Flow energetics. *J. Fluid Mech.* **360**, 295–340.

STILLINGER, D. C., HELLAND, K. N. & VAN ATTA, C. W. 1983 Experiments on the transition of homogeneous turbulence to internal waves in a stratified fluid. *J. Fluid Mech.* **131**, 91–122.

TAYLOR, G. I. 1935 Statistical theory of turbulence. *Proc. R. Soc. Lond.* A **151**, 421–478.

TOWNSEND, A. A. 1976 *The Structure of Turbulent Shear Flow*. Cambridge University Press.

WEBSTER, C. A. G. 1964 An experimental study of turbulence in a density-stratified shear flow. *J. Fluid Mech.* **19**, 221–245.

YEUNG, P. K., XU, S., DONZIS, D. A. & SREENIVASAN, K. R. 2004 Simulations of three-dimensional turbulent mixing for Schmidt numbers of the order 1000. *Flow Turbul. Combust.* **72**, 333–347.

YEUNG, P. K., XU, S. & SREENIVASAN, K. R. 2002 Schmidt number effects on turbulent transport with uniform mean scalar gradient. *Phys. Fluids* **14**, 4178–4191.